Material Modelling of Wood in Regard to Cutting Processes

Emrah Karakaya

Report No. xx-I-xx
Institut für Mechanik (Bauwesen) · Lehrstuhl I · Prof. C. Miehe
Universität Stuttgart, 70550 Stuttgart, Pfaffenwaldring 7, Germany

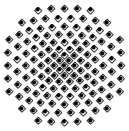

M. Sc. Thesis supervised by
Dr.–Ing. D. Rosato, M.Sc. and Prof. Dr.–Ing. C. Miehe at University Stuttgart
Tobias Hans and Sonja Rempler at Robert Bosch GmbH
Stuttgart, May 2011

Contents

1 Introduction

Wood is one of the oldest materials that human beings have used. The documented constructive use goes back for over 7000 years [1]. As a construction material, wood has good material and mechanical properties. It is strong in relation to its weight and it is a good heat/electrical insulator. It is easily machinable, it can be fabricated into a variety of shapes and sizes. Moreover, it is an economical, renewable and biodegradable resource.

In recent years, increasing attention is being devoted to the improvement of cutting practices of wood in the power tools industry. A better understanding of cutting process of wood contributes to optimizing cutting geometry, reducing tool wear, improving tool material and sizing tool-machines. Therefore, predictive methods and models for the simulation of material behavior covering wide ranges of flow stress, strain and high strain rate are needed in the area of cutting.

The aim of this work is to research existing approaches to metal cutting in order to define the needs and characteristics of the wood chipping and to present a view of the general requirements of such an environment. The next step is to identify the parameters of a selected material model through an optimization procedure using OptiSlang and to validate the model in comparison with measurements. In summary, a complete procedure of parameter identification method is aimed to be designed in order to simulate wood cutting regarding to industrial quality requirements.

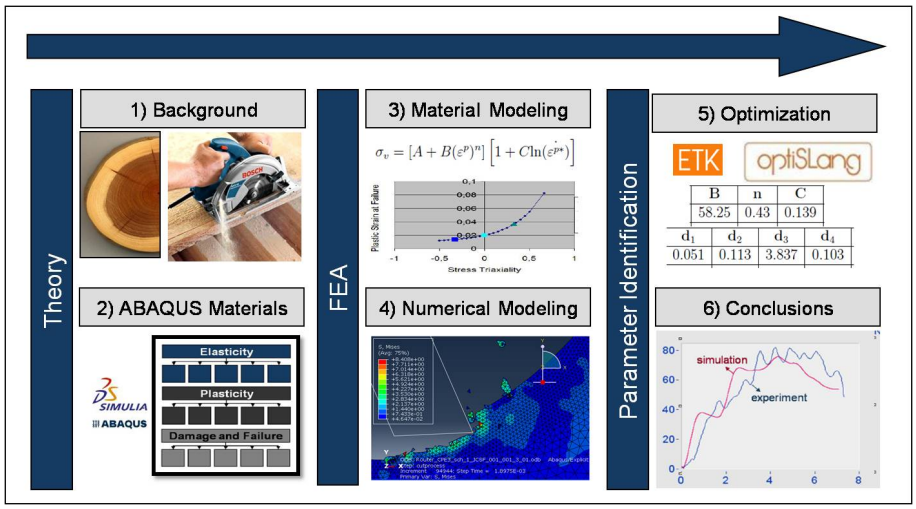

Figure 1: Overview of the sections for the Master Thesis

In this manner, the studies are divided into six parts which also construct the index of the thesis as presented in Figure 1. **Section 2** firstly gives information on required background to have a better understanding of the wood cutting modeling. This background starts with the material characteristics of wood in regard to wood anatomy and mechanical properties (Section 2.1) and it continues with the fundamentals of machining (Section 2.2) where the basics of wood cutting are explained. Then the basics of continuum mechanics and Finite Element Method (Section 2.3) are introduced in order to clarify the basis of explicit dynamic analysis for Finite Element Method. Finally, the arguments of parameter identification process is explained in Section 2.4 where the nonlinear optimization and parameter identification methods are introduced. After theoretical background,

the literature is researched and the material models in Abaqus libraries are analyzed in order to choose the best possible material model for wood cutting (**Section 3**). Because of the fact that there is not yet any material model which is able to predict cutting forces in wood cutting in literature, the literature research contained also area of metal cutting. After proposing a material model for wood cutting, the methodology of the numerical model is explained and the important challenges of cutting simulations are presented in **Section 4**. These important challenges of the numerical modeling are constructing the initial geometry (Section 4.1), reducing artificial energy (Section 4.2), deciding mesh size (Section 4.3) and filtering the cutting force curves (Section 4.4). Then parameter identification process is introduced in **Section 5** in four steps: experimental results, Finite Element modeling, parameter identification and validation. The parameters of proposed model are identified in regard two different experimental conditions. Then these identified parameters are used for simulating other two different experimental conditions in order to check the validity area of the parameters. Finally, in **Section 6**, the results are interpreted and recommendations for future work are presented. It should be considered that this study presents a whole methodology on how to model wood cutting and how to identify the parameters of the material model. In conclusion, the simulation results of router cutting for medium density fiberboards are matching with experiments and this indicates the potential of the material model and methodology for the future work.

2 Theoretical Background

2.1 Wood as an Engineering Material

In this sub-chapter firstly an overview of the anatomic structure and the mechanical properties of wood is presented. Kettunen [1] and Wood Hand Book [2] are for a more complete description of the structure and properties of wood. In addition, the brief reviews of mechanical properties of wood can be found in PhD Theses of Holmberg [3] and Neumann [4].

2.1.1 Anatomy of Wood

Wood is a cellular and anisotropic material [1, 5]. The degree of the structural anisotropy of the structure depends on the magnification at which the structure is described. The structure of wood can be described at macro level (discernible by naked eye), micro level (visible with the optical microscope) and cell wall level (visible with the electron microscope, so called ultrastructure).

The characteristic **macro-structure** of wood in the cross-section of a stem is formed by concentric annual rings (growth rings or xylem layer) as shown in Figure 2.

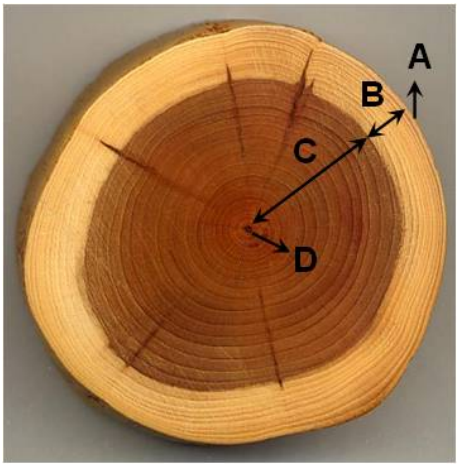

Figure 2: Cross-section of a Yew branch: (A) Bark and cambium (B) Sapwood (C) Heartwood (D) Pith (adopted from wikipedia [6])

The bark (A) is the outermost and consists of inner-bark (phloem) and outer-bark. Cambium (A) is between inner-bark and growth rings. Cambium is a very thin layer capable of producing new cells and therefore takes care of the lateral growth of the tree. Growth rings appear more clear in softwoods (conifer trees, for example pine) than hardwoods (deciduous trees, for example aspen and beech).
The outer section of growth rings is called sapwood (B) while the center section is called heartwood (C). Sapwood is responsible for nutrition transport from the roots to the leaves while heartwood consists of so called "dead" cells. The characteristic heartwood gives to the living tree stem stiffness and strength.

The growth rings are composed of two layers as shown in Figure 3. The brighter area of a growth ring is called earlywood and the darker area is called latewood. The layer of

earlywood is thicker than that of latewood that is found at the end of a growth season.

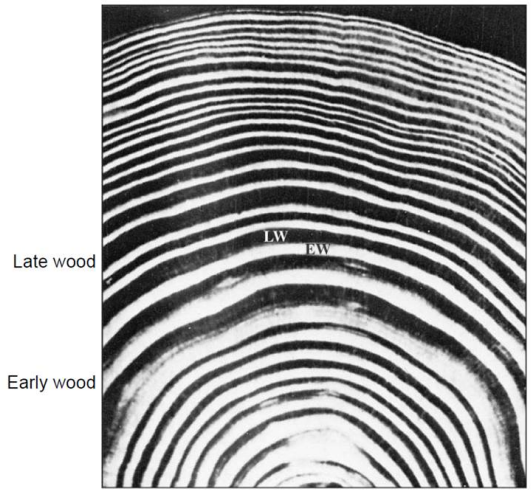

Figure 3: Latewood and earlywood (from Paulo Monteiro [7])

On the **microscopic level**, the structure of wood appears to consist of honeycomb type cells. The structure and the order of cells can be differentiated in softwoods and hardwoods as illustrated in Figure 4 and Figure 5.

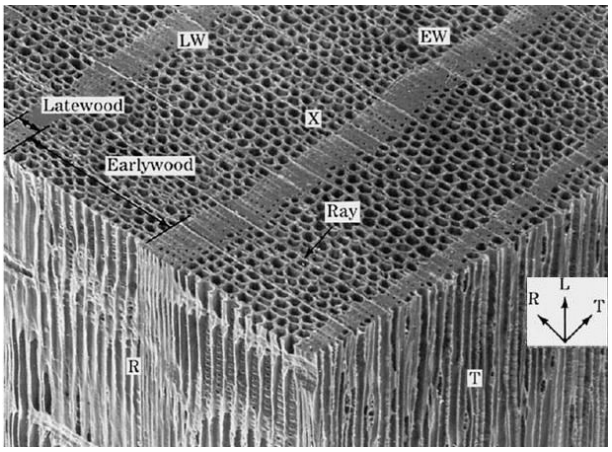

Figure 4: Micro-structure of softwood (according to Paulo Monteiro [7])

The basic cell structures appearing in softwoods and hardwoods are called tracheid and parenchyma. The other two cell types appear only in hardwoods and they are called fibers and rays. For a more complete description of wood micro-structure and in-depth investigation, reference is made to Kettunen [1].

On the **ultra structural level**, the cell walls appear to be composed of several layers. The scheme of the cell walls is illustrated in Figure 6. The outermost in the wall is called the primary wall and its abbreviation according to international nomenclature is P. Secondary wall (S) is below the primary wall (P) and it consists of three layers so called outer layer (S_1), middle layer (S_2) and inner layer (tertiary) (S_3 or T). Middle lamella is in between the cells and it serves as a bonding medium holding the cells together.

Wood has a cellular structure and can be classified as fiber reinforced polymer matrix composite [1]. Due to its cell structure, the most noticeable features are high anisotropy

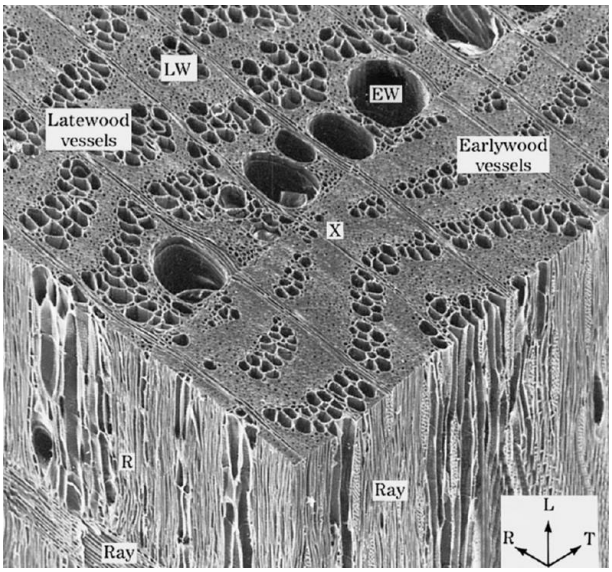

Figure 5: Micro-structure of hardwood (according to Paulo Monteiro [7])

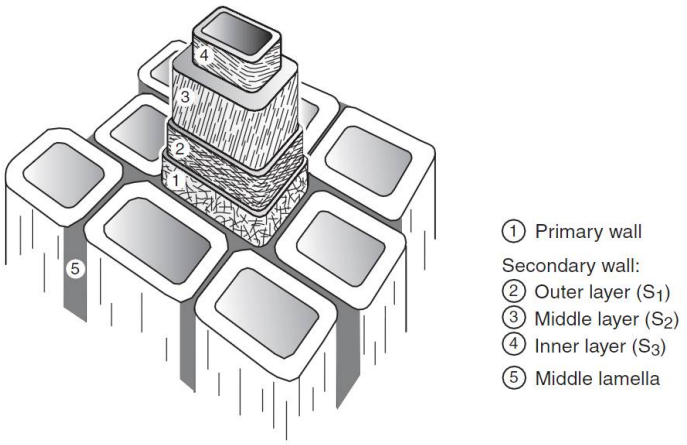

Figure 6: Ultrastructure of wood (according to Stefan Holmberg [3])

and different behavior under tension and compression. In the following, firstly the mechanical properties of wood are reviewed in the elastic and plastic regions including fracture mechanism, then the factors influencing these properties are presented.

2.1.2 Mechanical Properties

Wood is commonly assumed to be orthotropic because of the manner of tree growth and the arrangement of the cells [5, 8]. Wood possesses different properties in three principal directions, longitudinal (fiber direction) (L), tangential (T) and radial (R) as presented in Figure 7. The elastic stiffness matrix of an orthotropic material has nine independent constants. These nine elastic constants are E_{11}, E_{22}, E_{33}, G_{12}, G_{13}, G_{23}, ν_{12}, ν_{13}, and ν_{23}, where E is Young's modulus, G is shear modulus and ν is Poisson's ratio. In case of wood elasticity, subscript 1 refers to (L), subscript 2 refers to (T) and subscript 3 refers to (R). Therefore Hooke's generalized law for a linear elastic orthotropic material can be written as

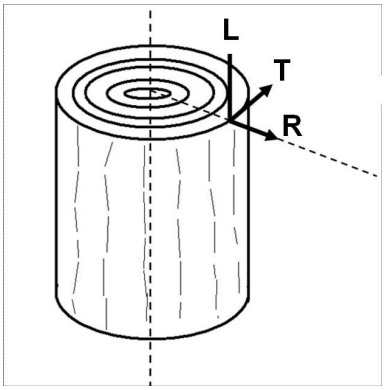

Figure 7: Longitudinal (L), tangential (T) and radial (R) directions

$$\sigma = C\varepsilon \tag{1}$$

or in the inverse form

$$C = D^{-1}, \tag{2}$$

$$\varepsilon = D\sigma \tag{3}$$

with the indices of three directions

$$\begin{bmatrix} \sigma_{11} \\ \sigma_{22} \\ \sigma_{33} \\ \sigma_{12} \\ \sigma_{23} \\ \sigma_{13} \end{bmatrix} = \begin{bmatrix} C_{1111} & C_{1122} & C_{1133} & 0 & 0 & 0 \\ C_{2211} & C_{2222} & C_{2233} & 0 & 0 & 0 \\ C_{3311} & C_{3311} & C_{3333} & 0 & 0 & 0 \\ 0 & 0 & 0 & C_{1212} & 0 & 0 \\ 0 & 0 & 0 & 0 & C_{2323} & 0 \\ 0 & 0 & 0 & 0 & 0 & C_{1313} \end{bmatrix} \begin{bmatrix} \varepsilon_{11} \\ \varepsilon_{22} \\ \varepsilon_{33} \\ 2\varepsilon_{12} \\ 2\varepsilon_{23} \\ 2\varepsilon_{13} \end{bmatrix} \tag{4}$$

or in the inverse form

$$\begin{bmatrix} \varepsilon_{11} \\ \varepsilon_{22} \\ \varepsilon_{33} \\ 2\varepsilon_{12} \\ 2\varepsilon_{23} \\ 2\varepsilon_{13} \end{bmatrix} = \begin{bmatrix} \frac{1}{E_{11}} & -\frac{\nu_{21}}{E_{22}} & -\frac{\nu_{31}}{E_{33}} & 0 & 0 & 0 \\ -\frac{\nu_{12}}{E_{11}} & \frac{1}{E_{22}} & -\frac{\nu_{32}}{E_{33}} & 0 & 0 & 0 \\ -\frac{\nu_{13}}{E_{11}} & -\frac{\nu_{23}}{E_{22}} & \frac{1}{E_{33}} & 0 & 0 & 0 \\ 0 & 0 & 0 & \frac{1}{G_{23}} & 0 & 0 \\ 0 & 0 & 0 & 0 & \frac{1}{G_{31}} & 0 \\ 0 & 0 & 0 & 0 & 0 & \frac{1}{G_{12}} \end{bmatrix} \begin{bmatrix} \sigma_{11} \\ \sigma_{22} \\ \sigma_{33} \\ \sigma_{12} \\ \sigma_{23} \\ \sigma_{13} \end{bmatrix} \tag{5}$$

where C is the symmetric constitutive matrix (called flexibility or compliance matrix also), D is the stiffness matrix, E is the modulus of elasticity, G is the shear modulus and ν is the Poisson ratio. The constitutive matrix is symmetric, which implies that

$$\frac{\nu_{23}}{E_{22}} = \frac{\nu_{32}}{E_{33}}, \tag{6}$$

$$\frac{\nu_{31}}{E_{33}} = \frac{\nu_{13}}{E_{11}}, \tag{7}$$

$$\frac{\nu_{12}}{E_{11}} = \frac{\nu_{21}}{E_{22}}. \tag{8}$$

Therefore there are nine independent elastic parameters describing the material behavior in the elastic region. If the wood is assumed as transversely isotropic material, the independent elastic constants reduce from nine to five with the relationships

$$E_{22} = E_{22}, \tag{9}$$

$$G_{12} = G_{13}, \tag{10}$$

$$\nu_{12} = \nu_{13} \tag{11}$$

where direction 1 (L) is the axis of symmetry. In addition, ν_{23} is not an independent constant due to isotropic plane. It can be calculated for example as

$$\nu_{23} = \frac{(E_{22} - 2G_{23})}{2G_{23}} \ . \tag{12}$$

The elastic moduli (E_{11}, E_{22}, E_{33}) of wood vary with different factors such as species, temperature, moisture but in general they have the following rational relation as presented in Table 1, Table 2 and Table 3

Table 1: The ratios of moduli of elasticity (from Holzphysik lecture notes [9])

	E_{11} (E_L)	:E_{22} (E_T)	:E_{33} (E_R)
softwoods	20	:1	:1.7
hardwoods	13	:1	:1.7

Table 2: The ratios of shear moduli (from Bodig and Jayne [10])

G_{13} (G_{LR})	:G_{12} (G_{LT})	:G_{23} (G_{TR})
10	:9.4	:1

Wood structure changes irreversibly when it is loaded beyond the elastic region. The strength values are influenced by several factors such as density, temperature, moisture or type of load. The most important structural factors according to Kettunen [1] are the fiber reinforcement and the geometric strengthening caused by the cell structure.

Table 3: The ratio of E_L and G_{LR} (from Bodig and Jayne [10])

E_L	:G_{LR}
14	:1

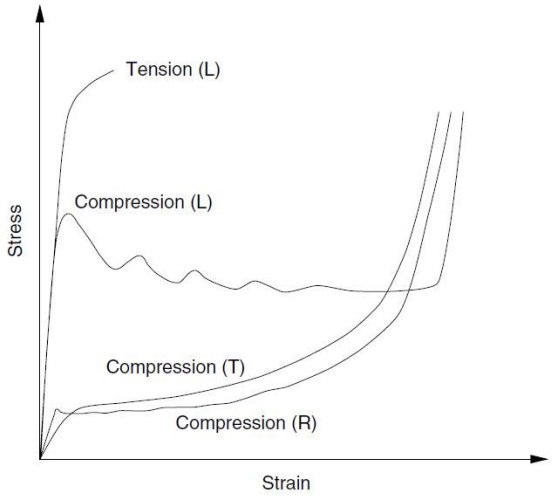

Figure 8: Typical stress-strain curves for wood loaded in compression(longitudinal, radial and tangential directions) and tension (longitudinal direction) (according to Stefan Holmberg [3])

Therefore strength values differ depending on the direction (longitudinal, tangential and radial) and type of load (tension, compression and bending). Typical stress-strain curves for dry wood loaded in different directions in tension and compression are illustrated in Figure 8.

According to Kettunen [1], wood can fracture in many different ways depending on the method of loading, direction of loading in relation to the cell structure etc. Fracture of wood consists of two steps called crack initiation and crack propagation. The crack propagation can be identified in eight different systems as presented in Figure 9.

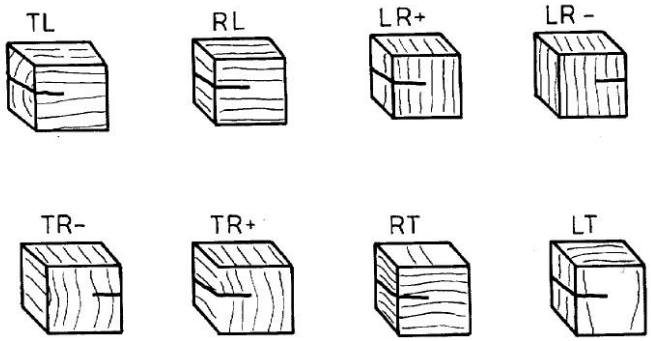

Figure 9: Crack propagation systems in wood (The distinction between them arises due to the asymmetric structure of the growth ring) (from Gibson and Ashby [11])

Crack propagation shows three types of behavior called Mode 1 crack (opening), Mode 2 crack (sliding) and Mode 3 crack (tearing) as presented in Figure 10. Therefore in woods

(considering the eight different systems of crack propagation) cracks might develop in 24 different ways.

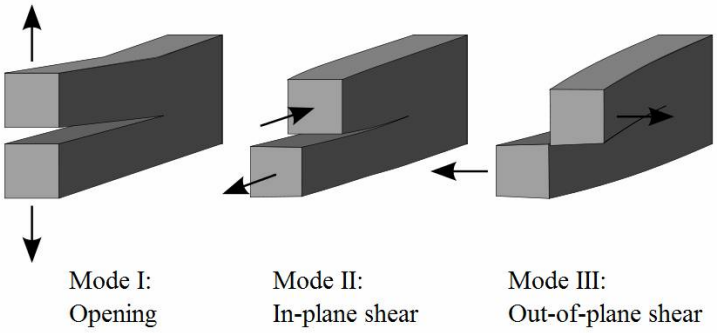

Figure 10: The three fracture modes (from wikipedia [**?**])

For the recent approaches for wood fracture and in-depth analyses, reference is made to Stanzl-Tschegg and Navi [12].

2.1.3 Factors Influencing the Mechanical Properties of Wood

A large number of factors influence the mechanical properties of wood. In the following, a number of important factors are presented. For a more complete description of the factors, reference is made to Kettunen [1].

Loading Method: The elastic moduli values are different under tension and compression in some wood species. However in some species such as Spruce, the difference is small and can be negligible. On the other hand, the strength properties depend also on the method of loading as seen in Figure 8. These different strength properties of some wood species can be seen in Table 4.

Table 4: The strength values of some wood species (according to DIN 68364)

Specimen of the wood	**Tension Strength** (MPa)	**Compression Strength** (MPa)
Beech ($Fagussylvatica$)	135	60
Spruce ($Piceaabies$)	65	45
Pine ($Pinussylvestris$)	100	47

Loading Direction: The strength and stiffness properties of wood depend on the orientation of loading, in other words the direction of external force in relation to the cell structure. For example, the moduli of elasticity and shear moduli of wood are considerably greater in the longitudinal direction than in the perpendicular directions (tangential and radial) due to the fact that fibers are oriented in longitudinal direction as seen in Table 1, Table 2 and Table 3).

Load Rate: The strength values of wood increase with the used loading rate (also with strain rate or stress rate). Figure 11 shows this relation in an indoor dry pine ($Pinussylvestris$).

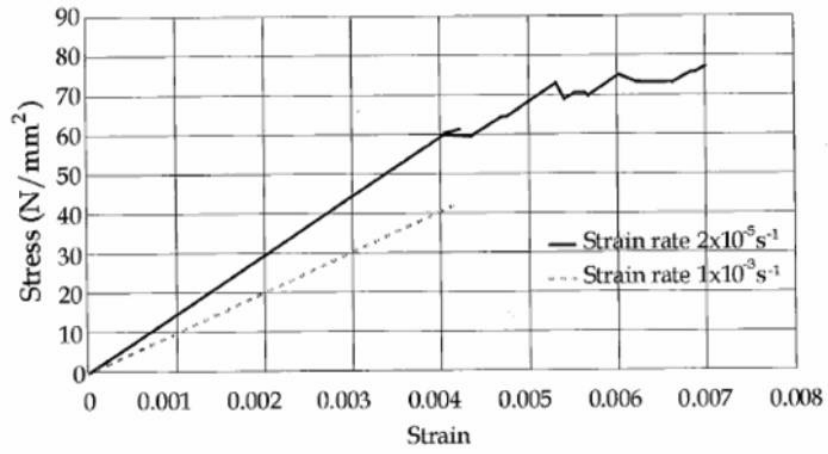

Figure 11: Influence of strain rate on the stress-strain curve of the sapwood of pine in tension. Moisture content of specimens is about 7% (from Kettunen [1])

Moisture: Wood is a hygroscopic material which absorbs water from its surroundings. Kettunen [1] states that the moisture content affects all the other strength values but not the axial tensile strength. Figure 12 presents the relation of the moisture content and strength of spruce (*Piceaabies*).

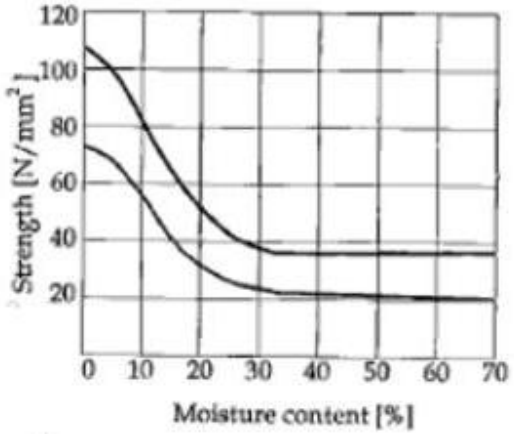

Figure 12: Nominal strength values of spruce as a function of moisture content. The upper curve indicates the ultimate bending strength and the lower one indicates the axial ultimate compression strength (from Kettunen [1])

Temperature: The influence of temperature depends on the moisture content of wood and it is most sensitive in tangential direction according to Kettunen [1]. In general, the stiffness and strength of wood decrease when it is heated and increase when it is cooled. Below approximately 150 °C, the relation of mechanical properties and temperature is approximately linear [2]. Figure 13 represents how temperature affects elastic and plastic properties.

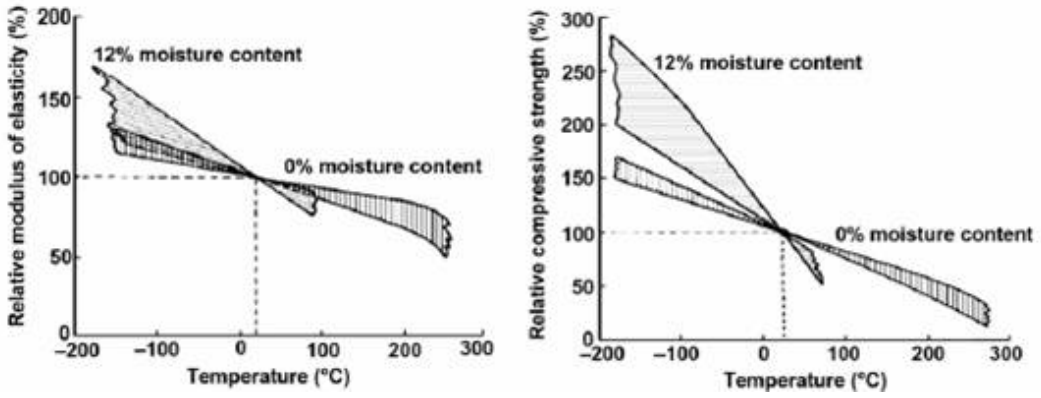

Figure 13: Effect of temperature in wood specimens (variability in reported trends is illustrated by width of bands). As a result of study of several investigators in Wood Hand Book [2]

2.2 Fundamentals of Machining

In this sub-chapter the term "machining" is introduced and types of machining are explained according to Geoffrey et al [13] and Niemz [9]. Furthermore, fundamentals of machining dynamics and vibration types in machining are briefly explained to give a basic idea of understanding the oscillations occurring in cutting force experiments. Finally in the last part of this sub-chapter, the fundamentals of wood cutting theory and the role of cutting forces are briefly described. The reference is made to the studies of Kivimaa (1950) [14], Franz (1958) [15] and Mckenzie (1960) [16] for the full description of the wood cutting theory. Furthermore the study of Marchal et al (2009) [17] is recommended for the complete review of the literature concerning wood cutting forces including the recent research approaches.

2.2.1 Classification

The term of machining can be defined as a collection of material-working processes in which power-driven machine tools with a sharp cutting tool are used to cut the material such as metal products, wood or plastic to achieve the desired geometry [18]. The principle of all these power-driven machine tools is to generate the surface required by suitable relative motions between cutting tool and the workpiece. This required relative motion can be decomposed into "primary motion" which causes relative motion between the tool and workpiece and "feed motion" which is provided by machine tool or manually in addition to primary motion to cause a repeated or continuous chip removal as shown in Figure 14 [13].

Classification of machining types can be done according to different criteria. For example, a wood machining classification based on the cutting edge and chip formation is presented in Figure 15 according to Niemz [9]. In this manner, some examples of wood cutting power tools are presented in Figure 16. Hand-held Circular saws (a), Routers (b) and Drill hammers (c) have a "geometrically definite cutting edge" causing arc-shaped chip and can be designed to cut different types of materials. For example, hand-held circular saws are mostly designed with a blade to cut wood but it is also possible to equip

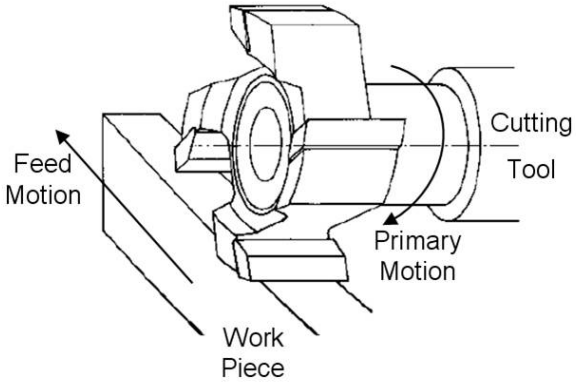

Figure 14: Primary and feed motion in Router (adopted from Niemz [9])

them with a blade designed to cut other types of materials such as metal or plastic. On the other hand, sheet-finishing sanders have a "geometrically indefinite cutting edge" and it smooths and finishes the material by abrasion with sandpaper. Depending mostly on the sandpaper, different materials (usually wood and wooden structures) can be shaped with sanders.

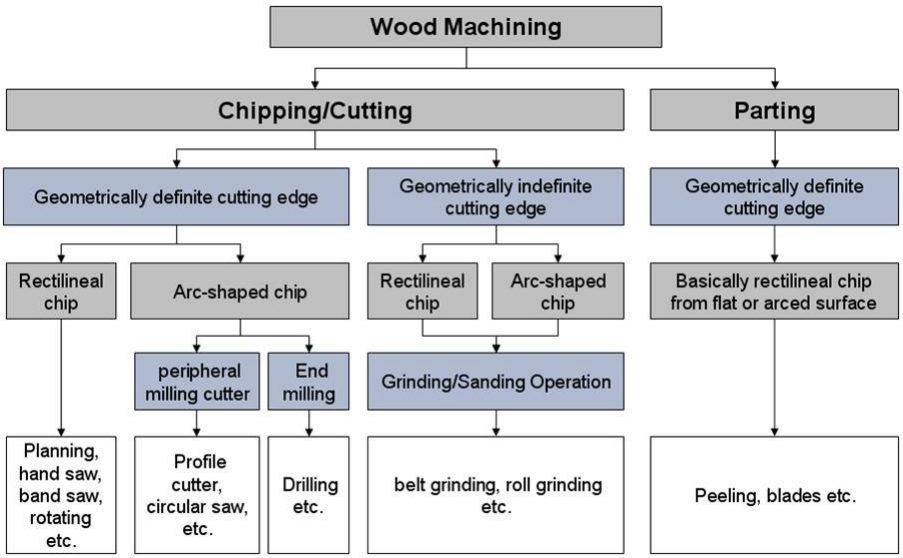

Figure 15: Classification of wood machining (adopted from Niemz [9])

2.2.2 Machining Dynamics

The machining and the machine dynamics within the machine system or with a power tool should be well understood and controlled where the quality of the precision machined surfaces or measuring cutting forces are important. The main issues affecting machining dynamics can be listed as the machine tool, the cutting tool, the workpiece, material and operation conditions. In this manner, it is important to know the causes and the effects of vibrations and chatter occurring in machining. Cheng [20] classifies the factors causing machining instability as chatter vibrations, random and free vibrations and forced vibra-

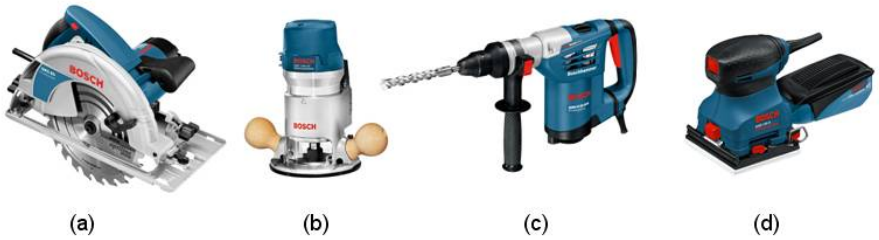

Figure 16: Some wood cutting tools, a) Hand-held circular saw, b) Router, c) Drill hammer, d) Sheet finishing sander (from Robert Bosch GmbH [19])

tion as shown in Table 5. The free vibrations regard to machine tool vibrations under pulsating excitations. According to Cheng [20], the origins of pulsating excitations in machine tools include

1) Cutter-contact forces when milling or flying cutting,
2) Inertia forces of reciprocating parts,
3) Vibrations transmitting from foundations,
4) Imperfections of materials.

Apart from free vibrations, if the vibration occurs during the presence of external energy source, it is called forced vibration; and if the vibration source lies in the system, it is called self-excited vibration which results in chatter vibration in the machine tool.

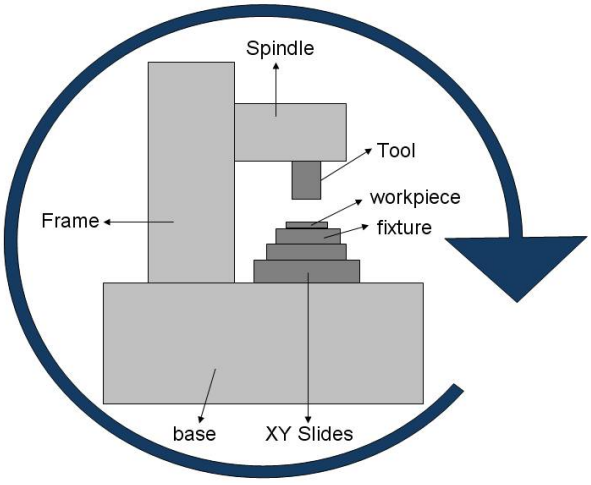

Figure 17: A typical machine-tool loop (adopted from Cheng [20])

In order to understand the physical formulation of vibrations, dynamic loop stiffness of a whole machine-tool system should be accurately predicted. Dynamic loop stiffness of machining system can be measured using an excitation load or can be calculated with the Finite Element Method in which expensive computational time is required due to the complexity of the system. In order to have a rough approximation, a simple method can be presented according to Cheng [20] for a sophisticated system including the cutting tool, the tool holder, slide ways and fixture etc. as shown in Figure 17.

Table 5: Classification of Machining Instability (adopted from Cheng [20])

	Dependency	**Location**	**Causes**	**Features**
Chatter Vibrations	Regenerative	Between cutting edge and workpiece	Overlapping cut	Self-excited vibration; leaves a wavy surface on workpiece
	Frictional	Tool flank-workpiece; chip-tool rake face	Rubbing on the flank face and the rake face	Self-excited vibration; amplitude depends on the system damping
	Mode coupling	In cutting and thrust force directions	Friction on the rake and clearance faces; chip thickness variation; shear angle oscillation	Mode coupling vibration; simultaneous vibration in two directions
Random and free vibrations	Tool	Tool flank-workpiece; chip-rake face	Tool wear and breakage	Random and chaotic; depends on cutting conditions
	Workpiece	Cutting zone	Material softening and hardening; hard grain and other kinds of flaws	Random and chaotic; depends on material property and its heat treatment
	Environment	Whole cutting processes	Environmental disturbances	Random and chaotic; depends on work environment
Forced vibration	Machine tool component	Whole cutting process	Off-balance of moving components, such as the spindle	Forced vibration

According to Cheng [20], a rough approximation of dynamic stiffness k_{dyn} and deformation x_{dyn} can be formulated as

$$x_{dyn} = \frac{\tilde{F}}{k_{dyn}}, \tag{13}$$

$$k_{dyn} = \frac{k_{static}}{Q} \tag{14}$$

where $\tilde{F}$ is the dynamic load applied to the machine tool, k_{static} is the static stiffness of the machine tool and Q is the amplification factor. k_{static} can be calculated as following in the case of a typical machine-tool loop

$$k_{static} = \frac{F}{x_{staticloop}} = \frac{1}{k_1} + \frac{1}{k_2} + ... + \frac{1}{k_n} + \frac{1}{k_1 + k_2 + ... + k_m} \tag{15}$$

where n indicates the total number of individual elements connected in series; m refers to the total number of individual elements connected in parallel in the machine-tool loop; F indicates the static and quasi static forces which normally come from gravity and cutting forces and $x_{staticloop}$ refers to static deformation. Furthermore, the amplification factor Q can be calculated from

$$Q = \frac{1}{2\zeta} = \frac{1}{2\frac{c}{2M\omega_0}} = \frac{M\omega_0}{c} \tag{16}$$

where M and c is the mass and damping. Moreover, the natural frequency ω_0 and damping ratio ζ can be calculated

$$\omega_0 = \sqrt{\frac{k_{static}}{M}}, \tag{17}$$

$$\zeta = \frac{c}{2M\omega_0} \tag{18}$$

and therefore

$$x_{dyn} = \frac{\tilde{F}}{k_{dyn}} = \tilde{F}\frac{1}{c}\sqrt{\frac{M}{k_{static}}}. \tag{19}$$

These formulations explained above show that dynamic loop stiffness is affected by all the components of a machine-tool loop, total mass and damping. In this manner and starting from dynamic loop stiffness which is derived finally in Equation 19, the reference is made to Cheng [20] in order to get the formulation of free and forced vibrations.

2.2.3 Orthogonal Wood Cutting

Orthogonal cutting is the fundamental research area in the wood cutting processes. It is a special case of cutting which means that the cutting edge is perpendicular to the relative motion of tool and workpiece in the machining process [21] as shown in Figure 18. Orthogonal cutting is widely used in theoretical and experimental work because of the fact that it presents a two-dimensional problem and it has less independent variables than a three-dimensional one. The first scientific work on orthogonal wood cutting with description of the formation and typology for chips goes back to 1950s with the studies of Kivimaa (1950) [14], Franz (1958) [15] and McKenzie (1960) [16].

In the scientific area of wood cutting analysis (also in orthogonal wood cutting), cutting force (R) is often chosen as the main output parameter to describe the process physically and this gives a better understanding of the phenomena occurring in wood cutting [17]. Marchal et al [17] indicate the possible reasons behind measuring the cutting forces in the wood cutting research area as the following

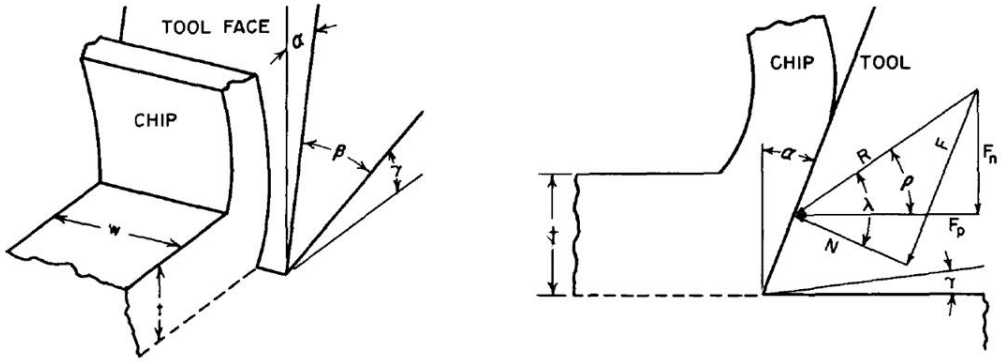

Figure 18: Cutting geometry and nomenclature in orthogonal cutting (from Woodson and Koch [21]) (**Definitions:** α - Rake angle; β - Sharpness angle; γ - Clearance angle; t - Thickness of undeformed chip; w - Width of undeformed chip; F_n - Normal tool force; F_p - Parallel tool force; R - Resultant tool force; ρ - Angle of tool force resultant; F - Friction Force; N - Normal to the friction force; λ - Angle between resultant tool force and the normal frictional force)

1) Understanding the machinability of different wood materials,
2) Resizing motors of machine tools to decrease energy consumption,
3) Optimizing the tool geometry,
4) Comparing the cutting properties of different tool materials,
5) Avoidance of dust and noise,
6) Improvement of productivity (increasing cutting speed etc.).

The cutting force, in other words the resultant force (R) occurring in orthogonal cutting can be decomposed in different ways. According to the Marchal et al [17], decomposition into parallel and normal components is suitable from the technological point of view and this way is mostly used in the wood cutting research area. In this manner, the geometry concerning the orthogonal cutting and the decomposition of resultant force into parallel and normal components is presented in Figure 18.

The study of Palmqvist [22] indicates that the parallel component of the tool force (so called parallel cutting force, F_p) gives the information on the torque and the energy consumption while the normal component of the tool force (so called normal cutting force, F_n) gives the information on cutting refusal tendency and tool wear. The following equation gives the relation between F_p and F_n, where R is resultant force

$$R = \sqrt{F_n^2 + F_p^2} \, . \tag{20}$$

In orthogonal cutting, it is possible to define 10 different cutting directions concerning the wood type. In this manner, the cutting direction describes the orientation between the cutting tool and wood sample. These different orthogonal cutting types are illustrated in Figure 19.

For solid woods, there are three main cutting directions specified with respect to grain

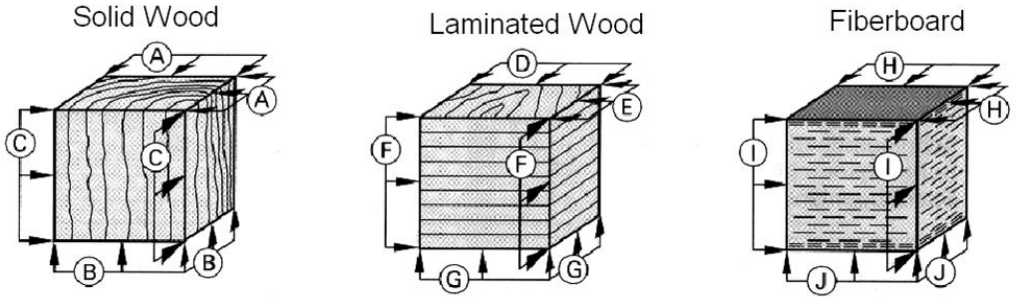

Figure 19: Orthogonal cutting directions for solid wood, laminated wood and fiberboard (adopted from Kivimaa [14] and Niemz [23]) (**Definitions: A**: Cutting direction is $\perp$ to fiber direction; cutting plane is $\perp$ to fiber direction (90°-90°), **B**: Cutting direction is $\parallel$ to fiber direction; cutting plane is $\parallel$ to fiber direction (90°-0°), **C**: Cutting direction is $\perp$ to fiber direction; cutting plane is $\parallel$ to fiber direction (0°-90°), **D**: Cutting direction is $\parallel$ to fiber direction; cutting plane is $\parallel$ to upper surface area, **E**: Cutting direction is $\perp$ to fiber direction; cutting plane is $\parallel$ to upper surface area, **F**: Cutting direction is $\parallel$ to layers, **G**: Cutting direction is $\perp$ to layers, **H**: Cutting direction is $\parallel$ to upper surface area, **I**: Cutting direction is $\parallel$ to fiber orientation, **J**: Cutting direction is $\perp$ to fiber orientation.)

direction, so called 90°-90° (A) , 90°-0° (B) and 0°-90° (C) [15]. In this designation, the first number describes the angle between the cutting edge and the grain direction and the second number the angle between the direction of cutting and grain direction.

For example in 90°-0° orthogonal cutting, three basic chip types can be observed according to Hoadley [24]. Type 1 refers to the cutting at larger cutting angles α (rake angle); type 2 refers to the cutting at small cutting angles and finally type 3 refers to the cutting at very small or even negative cutting angles as shown in Figure 20. The type 1 chip formation can be understood better with decomposition of process into four parts involving a cyclic sequence. Firstly (A) (see Fig. 20), the cutting tool separates the fibers and the separated chip slides up the cutting tool. Next, the fracture of wood in tension perpendicular to grain occurs and therefore the chip lengthens itself (B). When the bending stresses equal the strength of wood, the chip breaks (C) and finally the cutting edge advances to the failure point (D) and therefore the cyclic sequence goes to the first step again (A) [24]. At smaller angles (type 2), the component of upward lifting transmitted to chip gets smaller and failure occurs as a diagonal plane of shear with the component of forward compression. Finally, at very small cutting angles (type 3) , the component of forward compression is much greater and it causes the compressional failure in wood.

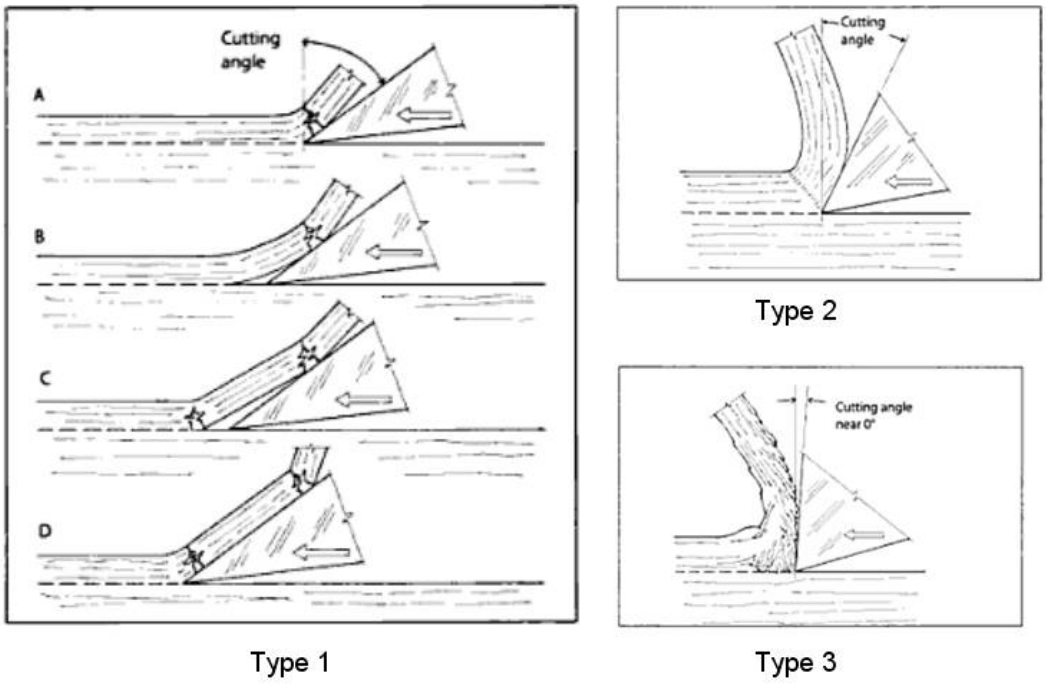

Figure 20: Three basic chip formation occuring in 90°-0° orthogonal cutting (from Hoadley [24])

2.3 Background to Finite Element Method

In this chapter a basic formulation of elastic and inelastic problems in conjunction with continuum mechanics and Finite Element Method (FEM) is briefly described. The formulation of fundamentals of continuum mechanics is based on the lectures of Miehe [25, 26]. The formulation of mechanical constitutive modeling and the explicit dynamics analysis is based on the Abaqus Theory Manual [27]. For a complete description including the formulation about the further themes, reference is made to Miehe [25, 26] and Hughes et al [28].

2.3.1 General Introduction to Continuum Mechanics

The material body $\mathfrak{B}$ is an idealized physical object where the material points are defined. The body $\mathfrak{B}$ occupies a domain B in the Euclidean space R^3. The Euclidean space has two configurations. These two configurations can be called in three different ways

$$B : \begin{cases} \text{"Reference Configuration"} \\ \text{"Langrangian Configuration"} \\ \text{"Material Configuration"} \end{cases} , \; S_t : \begin{cases} \text{"Current Configuration"} \\ \text{"Eulerian Configuration"} \\ \text{"Spatial Configuration"} \end{cases}$$

Based on the configuration presented in Figure 21, the nonlinear deformation map φ_t is defined as

$$\varphi_t : \begin{cases} B \rightarrow S_t \\ \boldsymbol{X} \rightarrow \boldsymbol{x} = \varphi_t(\boldsymbol{X}) \end{cases} . \tag{21}$$

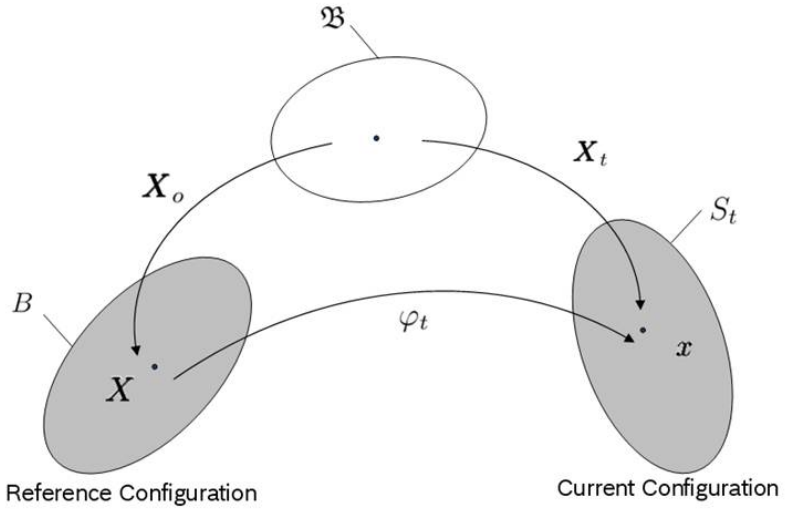

Figure 21: Nonlinear deformation map between reference and current configuration

Between the reference and current configuration, three basic mappings are defined. Firstly the Frechet derivative of the deformation map φ_t defines the deformation gradient $\boldsymbol{F}$ and it maps tangent vectors $\boldsymbol{T} \in T_X B$ to material curves onto tangent vectors $\boldsymbol{t} \in T_x S_t$ of the deformed curves where $T_X B$ and $T_x S_t$ are the tangent spaces of the manifolds B and S_t at $\boldsymbol{X}$ and $\boldsymbol{x}$ respectively.

$$\boldsymbol{F} = \nabla_X \varphi_t(\boldsymbol{X}) \tag{22}$$

The cofactor of the deformation gradient $\operatorname{cof} \boldsymbol{F}$ maps normal vectors $\boldsymbol{N} \in T_x^* B$ onto the deformed normal $\boldsymbol{n} \in T_x^* S_t$ where $T_x^* B$ and $T_x^* S_t$ are cotangent spaces of B and S respectively.

$$\operatorname{cof} \boldsymbol{F} = \det[\boldsymbol{F}] \boldsymbol{F}^{-T} \tag{23}$$

Finally, the determinant of the deformation gradient J maps volume elements from the reference to the current configuration.

$$J = \det[\boldsymbol{F}] > 0 \tag{24}$$

The visualization of these three basic mappings are illustrated in Figure 22.

According to Cauchy‘s Theorem, the true (Eulerian) traction vector (force per unit area) $\boldsymbol{t} \in T_x S_t$ is assumed to be a linear function of the normal vector $\boldsymbol{n} \in T_x^* S_t$

$$\boldsymbol{t} = \boldsymbol{\sigma n} \tag{25}$$

where $\boldsymbol{\sigma}$ represents the true Cauchy‘s tensor and Cauchy-like theorem defines

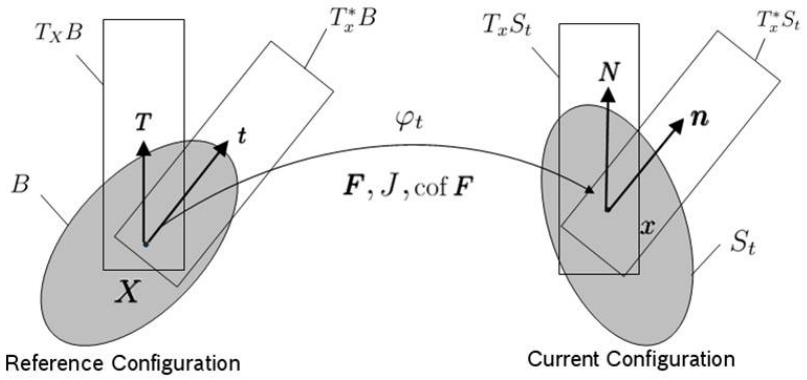

Figure 22: 3 basic deformation maps with tangent and cotangent spaces

$$\boldsymbol{T} = \tilde{\boldsymbol{P}}\boldsymbol{t} \tag{26}$$

where $\tilde{\boldsymbol{P}}$ represents nominal First Piola-Kirchhoff tensor which gives the force measured per unit area in the reference configuration.

2.3.2 Mechanical Constitutive modeling

The mechanical material response can be decomposed into two parts called "elastic response" and "inelastic response". The elastic and inelastic responses are distinguished from each other by separating the deformation into recoverable (refers to elastic response) and nonrecoverable (refers to plastic response) parts [27]. This separation is based on the local multiplicative decomposition within the neighborhood N_x of $X \in B$ as shown in Figure 23. Therefore the deformation gradient can be decomposed as

$$\boldsymbol{F} = \boldsymbol{F^e F^p} \tag{27}$$

where $\boldsymbol{F^e}$ and $\boldsymbol{F^p}$ are called elastic and plastic deformation maps (not gradients) respectively. Equation 27 can be used directly to formulate the plasticity model [27] and

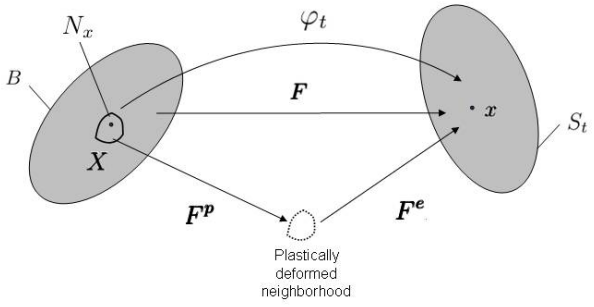

Figure 23: Decomposition of deformation gradient

therefore an additive strain rate decomposition can be written as

$$\dot{\boldsymbol{\varepsilon}} = \dot{\boldsymbol{\varepsilon}}^{\boldsymbol{e}} + \dot{\boldsymbol{\varepsilon}}^{\boldsymbol{p}} \tag{28}$$

where $\dot{\boldsymbol{\varepsilon}}$, $\dot{\boldsymbol{\varepsilon}}^{\boldsymbol{e}}$ and $\dot{\boldsymbol{\varepsilon}}^{\boldsymbol{p}}$ refer to the total strain rate, the elastic strain rate and the plastic strain rate respectively. The Equation 28 is assumed for the inelastic response models of Abaqus and it is a consistent approximation to Equation 27 (see Abaqus Theory Manual section, 1.4.4 [27] for further information) when the elastic strains are infinitesimal and when strain rate is the rate of the deformation as (where $\boldsymbol{v}$ refers to spatial velocity)

$$\dot{\boldsymbol{\varepsilon}} = sym(\dot{\boldsymbol{F}}\boldsymbol{F}^{-\mathbf{1}}) = sym\left[\frac{\partial \boldsymbol{v}}{\partial \boldsymbol{x}}\right] \tag{29}$$

In many materials such as metals, Equation 28 is consistent since the elastic strains remains very small in these materials. However for some materials such as polymers, this approximation is not consistent since they undergo large elastic strains. The simplest elasticity provided in Abaqus is linear elasticity:

$$\boldsymbol{\sigma} = \boldsymbol{D}^{\boldsymbol{e}} : \boldsymbol{\varepsilon}^{\boldsymbol{e}} \tag{30}$$

This elasticity model is used either for small-strain elasticity problems or to model elasticity in an elastic-plastic model in which elastic strains are always small. Moreover, two of the other kinds of elasticity models provided in Abaqus called "hypoelastic" and "hyperelastic" models. In hypoelastic model, the strains still remain small but elasticity may be nonlinear. The behavior is described as

$$\dot{\boldsymbol{\sigma}} = \boldsymbol{D}^{\boldsymbol{e}} : \dot{\boldsymbol{\varepsilon}}^{\boldsymbol{e}} \ . \tag{31}$$

A hyperelastic model is a nonlinear elastic behavior where the stress $\boldsymbol{\sigma}$ (true Cauchy tensor, see Equation 25 is derived from strain energy density potential U

$$\boldsymbol{\sigma} = \frac{\partial U}{\partial \boldsymbol{\varepsilon}} \tag{32}$$

which is generally used to model materials whose long-term response to large deformations is fully recoverable (such as elastomer). Apart from elastic response, the plastic response in materials also can be described with the strain energy density potential as

$$\boldsymbol{\sigma} = \frac{\partial U}{\partial \boldsymbol{\varepsilon}^{\boldsymbol{e}}} \ . \tag{33}$$

2.3.3 Explicit Dynamics Analysis

Starting from the equilibrium of force and moment for displacement problems, the Finite Element Method is based on so called Virtual Work equation in the classical form (See Zienkiewicz et al [29] and Belytschko et al [30] for the fundamental formulation of FEM):

$$\int_V \boldsymbol{\sigma} : \delta\boldsymbol{\varepsilon} dV = \int_S \boldsymbol{t}^T . \delta\boldsymbol{u} dS + \int_V \boldsymbol{f}^T . \delta\boldsymbol{u} dV \tag{34}$$

where V is a volume occupied by a part of the body in the current configuration, S is the surface bounding this volume, $\boldsymbol{f}$ is the body force at any point within the volume and $\boldsymbol{\sigma}$ is the Cauchy tensor which is described formerly in Equation 25.

Abaqus is designed as a tool for Finite Element modeling and it allows the user to step through the history to be analyzed [27]. The explicit dynamics analysis procedure in Abaqus/Explicit uses the explicit central difference integration rule for the motion of the body where the time incrementation is controlled by the stability limit of the central difference operator [27]. The explicit central difference integration rule can be written as

$$\dot{\boldsymbol{u}}^{(i+\frac{1}{2})} = \dot{\boldsymbol{u}}^{(i-\frac{1}{2})} + \frac{\Delta t^{(i+1)} + \Delta t^{(i)}}{2} \ddot{\boldsymbol{u}}, \tag{35}$$

$$\boldsymbol{u}^{(i+1)} = \boldsymbol{u}^{(i)} + \Delta t^{(i+1)} \dot{\boldsymbol{u}}^{(i+\frac{1}{2})} \tag{36}$$

where $\boldsymbol{u}$, $\dot{\boldsymbol{u}}$ and $\ddot{\boldsymbol{u}}$ are displacement, velocity and acceleration, respectively. The superscript $^{(i)}$ refers to the time increment number where $^{(i-\frac{1}{2})}$ and $^{(i-\frac{1}{2})}$ are mid-increment values. The stability of explicit procedures depends on the time incrementation that is used in central difference operation. The stability limit of time incrementation is limited in terms of highest eigenvalue in the system ω_{max} as

$$\Delta t \leq \frac{2}{\omega_{max}} \ . \tag{37}$$

In order to control high frequency oscillations, a small amount of damping is introduced in Abaqus/Explicit with the fraction of critical damping in the highest mode ξ as

$$\Delta t \leq \frac{2}{\omega_{max}} (\sqrt{1+\xi^2} - \xi) \ . \tag{38}$$

Abaqus/Explicit computes a trial time increment for each element in the mesh and defines the global time increment based on the most critical element in the mesh. In this manner, a trial increment for a element can be written as

$$\Delta t = \frac{2}{\omega_{max}^{element}} \tag{39}$$

where $\omega_{max}^{element}$ is the element maximum eigenvalue. The above equation can be written within a conservative estimation as

$$\Delta t = min(\frac{L_e}{c_d}) \tag{40}$$

where L_e and c_d refer to the characteristic element dimension and current effective dilatational wave speed of the material, respectively. Therefore, the size of the most critical element in the mesh affects the computational time/expenses due to the fact that one of the causes of higher computational cost is very small time increments.

2.4 Method of Parameter Identification

In this sub-chapter an overview of the fundamentals of nonlinear optimization and parameter identification is given. The theory of this sub-chapter is based on the lecture notes of Miehe [31] at University of Stuttgart, OptiSlang documentation [32] and PhD Theses of Rieger [33] and Scheday [34].

2.4.1 Nonlinear Optimization

Optimization is a fundamental task in all natural and engineering sciences [33] and it is defined as a procedure to achieve the best outcome of a given function while satisfying the given restrictions [32]. An optimization problem (such as a parameter identification problem) is characterized by an objective function $f(\boldsymbol{k})$, where $\boldsymbol{k}$ is a vector of parameters (so called optimization variables), with nonlinear equality and inequality constraints $\boldsymbol{g}$ and $\boldsymbol{h}$:

$$\left.\begin{array}{c} f(\boldsymbol{k}) \rightarrow min \\ h_i(\boldsymbol{k}) = 0,\ i = 1, ..., n_h \quad ; \quad g_i(\boldsymbol{k}) \leq 0,\ i = 1, ..., n_g \end{array}\right\} \tag{41}$$

The range of the variables $\boldsymbol{k}$ is limited by upper and lower bounds P. These boundaries are usually based on either physical context or practical knowledge:

$$P = a_i \leq k_i \leq b_i\ ,\ i = 1, ..., n \tag{42}$$

Current optimization techniques can be classified according to different point of views. One of the possible classifications is based on whether the technique uses the information of gradient or not and the other possibility depends on whether the experiments are deterministic or stochastic. These classifications of some well-known methods are presented in Table 6 and 7.

Table 6: Classification of optimization strategies in regard to gradient dependency (from Rieger [33])

Gradient Based Methods	**Gradient-Free Methods**
Gauss-Newton	Simplex strategies
Levenberg-Marquardt	Evolutionary algorithms
Quasi-Newton	
Sequential quadratic programming	

For example, **Quasi-Newton methods** try to find the minimum of the objective function by searching the zero point of the gradient function [32]. First the gradient of the objective function is calculated generally with central difference equations or single sided difference quotients. Next a Newton iteration is used for searching the zero point of the gradient function [32]. It should be considered that the objective function should be differentiable in all possible points in given design space. **Response Surface Method**

Table 7: Optimization Strategies Classification based on deterministic and stochastic methods (adopted from Optislang documentation [32])

Deterministic	**Stochastic**
Hill climbing methods	Markov process procedures
Simplex strategies	- Monte-Carlo
Complex strategies	- Importance sampling
Response Surface Methodology	Physical process procedures
Gauss-Newton	- Simulated annealing
Levenberg-Marquardt	- Tunneling algorithm
Quasi-Newton	Artificial life approach
Sequential quadratic programming	- Evolutionary algorithms
	- Neural network approach
	- Fuzzy network approach

(RSM) is a statistical method to construct smooth approximations (in general polynomial least square approximation or moving least square approximation) to functions in a multidimensional space [32]. **Evolutionary Algorithms (EA)** are suitable for all the cases where gradient based methods and RSM fail. EAs are stoschastic search methods that mimic processes of natural biological evolution. The main operators of EA consist of selection, reproduction, mutation and replacement [32].

2.4.2 Nonlinear Parameter Identification

Engineering applications often require the simulation of the deformation and failure behavior of structures at which precise prediction of the material response under various loading conditions has a key importance.

Table 8: Steps of parameter identification (adopted from Rieger [33])

Step	**Explanation**
1. Concept	Determination of observation scale (macro, micro, ultra) Characterization of phenomena (nonlinearities, hardening, failure, ...) Description of limitations for time, cost and experimental facilities
2. Numerical Modeling	Definition of phenomena with differential equations and introduction of material parameters $\boldsymbol{k}$
3. Parameter Identification	Identification of material parameters $\boldsymbol{k}$ in regard to data D_1
4. Verification	Investigation of the model quality in regard to data D_1
5. Validation	Investigation of the validity area of the material parameters in regard to a new data D_2

The steady increase of computational power allows for the numerical implementation of complex material models, for which often large sets of material parameters must be identified. Experimental data serves the important purpose of building the basis for

the precise fitting of material parameters as well as the validation of material models. Starting from this point, parameter identification consists of determination of the optimal parameter set through the best possible correlation of simulation and experimental data for a given material model. After the correlation of experimental and simulation data, the area of the validity for the identified parameters must be investigated. This validation process is based on new experimental and simulation data. In this manner, the steps of parameter identification method are presented in Table 8.

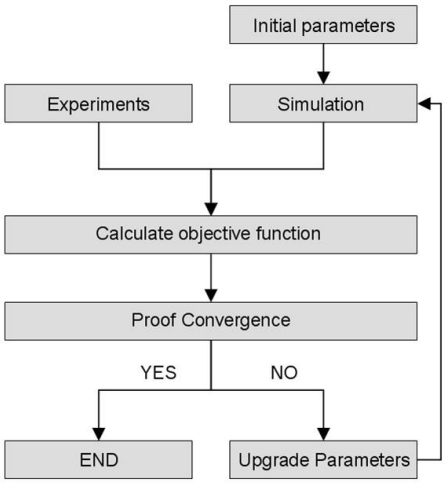

Figure 24: Flow chart of parameter identification (adopted from Rieger [33])

In order to operate a parameter identification process, definition of algorithm (which is usually implemented through a commercial optimization tool) is required. A schematic flow chart for parameter identification is illustrated in Figure 24. The step of "upgrade parameters" consists of one of the optimization types from the gradient based, gradient free, stochastic or deterministic methods (see Chapter 2.4.1 for the fundamental explanations of optimization methods). In alternative to proof convergence, the maximum number of iterations can also be used to stop the algorithm concerning the computational costs. It should be considered that the equation of objective function and the parameters given in Figure 24 present a random example. The objective function should be re-designed in regard to the specifications of the problem and the parameters.

2.4.3 Direct and Inverse Modeling Problems

In material modeling, the direct problem involves the computation of the material response based on the material model, material parameters, loading sequence and initial conditions [31] and it can be formulated as

$$find\ \boldsymbol{u}^{*}\ such\ that\ z(\boldsymbol{k},\boldsymbol{f},\boldsymbol{u}) = 0\ for\ given\ \boldsymbol{k}\ and\ \boldsymbol{f} \tag{43}$$

where $\boldsymbol{u}^{*}$ refers to material response and $z(\boldsymbol{k},\boldsymbol{f},\boldsymbol{u})$ refers to given model description with parameter set $\boldsymbol{k}$ and loading $\boldsymbol{f}$. On the other hand, the inverse problem in the context of parameter identification involves the search for optimal parameters for given

material model, loading sequence, initial conditions and known material response. The formulation of inverse problem can be written as

$$find\ \boldsymbol{k^*}\ such\ that\ z(\boldsymbol{k}, \boldsymbol{f}, \boldsymbol{u}) = 0\ for\ given\ \boldsymbol{f}\ and\ \boldsymbol{u}(\boldsymbol{k}) = \boldsymbol{u^{exp}}\ . \tag{44}$$

The difference between direct and inverse problems is whether the material parameters or material response are used as input or not in the given problem as shown at the graphical illustration in Figure 25. Material parameters are served as input in inverse problem while these parameters appear as output in the inverse problem of parameter identification process.

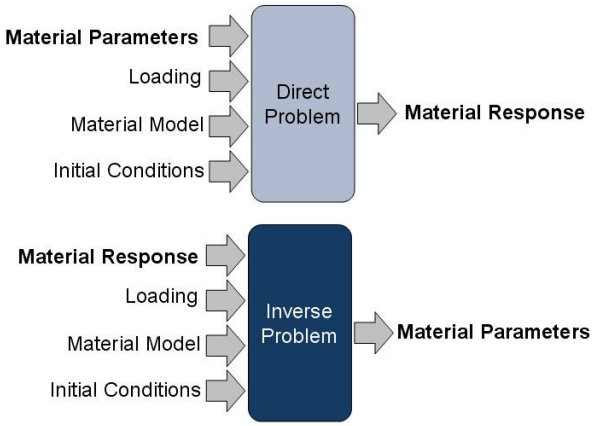

Figure 25: Direct and inverse problems (adopted from Rieger [33])

In the frame of master thesis, the parameter identification method is based on an inverse problem. The aim is going to be to identify the **material parameters** (the parameters of proposed model) for **a material model** (proposed model) using the **initial conditions** (experimental conditions), **loading** (experimental conditions) and **material response** (force-time curves).

3 Material Modeling in Cutting Processes

3.1 Literature Review

In the area of Finite Element Analysis (FEA), there is not yet any published scientific work about the material modeling of wood in cutting processes which is capable of predicting the physical phenomena such as cutting forces. The only studies related to wood cutting modeling are presented by McCallion et al [35] (2000) and Caugley et al (2003) [36]. The hybrid cellular/macroscopic models presented in these studies are able to identify failure mechanism in severing wood fibers during cutting but the conclusions of the studies do not reveal the validation of the models. Particularly, the studies about material modeling of wood are limited to quasi-static conditions or different dynamic processes such as impact and crash. In order to develop an approach to model wood in cutting processes, the possibilities of material modeling in cutting process for different materials (metals and cortical bones) are firstly investigated.

In metal cutting, the material is plastically deformed in deformation zone by simultaneous action of large compressive and shearing stresses while high temperatures occur due to the friction forces and dissipative plastic work [37]. In FEA of metal cutting, the requirements could be summarized according to Svoboda et al [37] as

1) Thermo-mechanical coupling
2) Friction modeling
3) Contact definition
4) Material modeling
5) Material removal definition

In this manner, Svoboda et al [37] indicates the most important numerical problems in modeling of metal cutting process as

1) Need of remeshing and contact algorithms (in case of eulerian modeling)
2) Dependency of the solution of cutting forces and chip formation on time stepping and element size in the mesh domain
3) Lack of experimental setup capable of high strain rates (SHPB is for strain rates up to 9000 s^{-1})

During recent decades, material modeling has been one of the more challenging research topics in metal cutting processes. Kalhori, Wedberg and Lindgren (2010) [38] indicate the need of reliable material models which are capable of predicting the thermo-mechanical behavior of materials at very high strain rates and high temperatures occurring in metal cutting processes. According to Kalhori et al [38], material models in metal cutting simulations can be classified into two groups starting from the point of view whether the material model is physically described or not as illustrated in Figure 26. The first group of models is called "empirical models". In the majority of commercial codes and scientific works related to metal cutting, the material behavior is described with empirical models (such as Johnson Cook Model [39]) at which the flow stress is defined in terms

of plastic strain, temperature and strain rate. Because of the fact that these empirical flow stress models are not based on any physical reasoning, their predictive capability depends on the experimental conditions at which the material parameters are identified. On the other hand, there are some studies investigating the predictive "physical material models" which constitute the second category. The studies of Svoboda, et al (2010) [37] and Kalhori et al (2010) [38] are the recent examples of these physical material models for metal cutting processes. However, physically based modeling for metal cutting is a new research area and it must be still feasible for large scale computations [37].

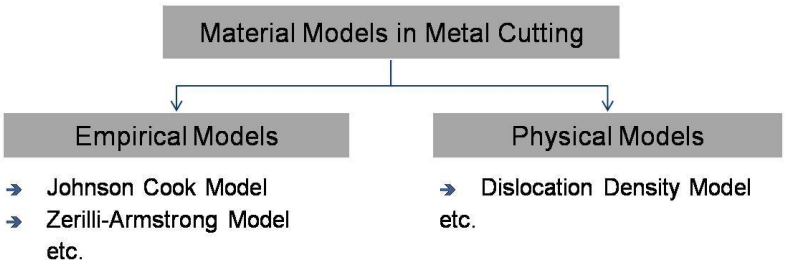

Figure 26: Classification of material models in metal cutting

Table 9: Experiment types used for obtaining material parameters in dynamic processes

Authors	**Year**	**Material**	**Process to be simulated**	**Experiment Type to obtain parameters**
O. Ghouati , J.C. Gelin [40]	1998	metal	metal forming processes	Tensile Test and deep drawing test
A. Maurel et al [41]	2008	304L steel	Milling	Tension test, Hopkinson Bar Tests, cutting Experiments
F.Chinesta, L.Fillice et al. [42]	2008	AISI 1045 steel	Machining	Machining
K.Alam, A.V. Mitrofanow et al. [43]	2009	Cortical bone	Plane cutting	Tension
Aviral Shrot, Martin Baeker [44]	2010	AISI 52100, 62 HRC steel	machining	machining
S.L. Sooa, D.K. Aspinwal et al.[45]	2004	AISI 52100, 62 HRC steel	Cutting	Uniaxial Compression and Cutting

Johnson Cook Material model is the most commonly used material model in metal cutting [46]. It is a particular type of Mises plasticity model consisting of analytical forms of the hardening law and rate dependency. It describes the flow stress σ (von Mises flow stress) as the product of plastic strain ε^p, plastic strain rate $\dot{\varepsilon^p}$ and temperature T [39]:

$$\sigma = [A + B(\varepsilon^p)^n] \left[1 + C\ln(\dot{\varepsilon^{p*}})\right] [1 - (T^*)^m] \tag{45}$$

where A, B, n, C and m are the material parameters. $\dot{\varepsilon^{p*}}$ refers to dimensionless plastic strain rate and is defined as

$$\dot{\varepsilon^{p*}} = \frac{\dot{\varepsilon^{p}}}{\dot{\varepsilon_0}}. \tag{46}$$

where $\dot{\varepsilon_0}$ refers to reference strain rate. T^* refers to dimensionless temperature and it is defined as

$$T^* = \begin{cases} 0 & \text{for} \quad T < T_t, \\ \dfrac{T - T_t}{T_m - T_t} & \text{for} \quad T_t \leq T \leq T_m, \\ 1 & \text{for} \quad T > T_m \end{cases} \tag{47}$$

where T is the current temperature, T_m is the melting temperature and T_t is the transition temperature. The Johnson Cook Model is recently used also for cutting simulations for cortical bones such as the study of Alam et al (2009) [43] at which the model was capable of predicting the cutting forces for various process parameters.

In order to identify the parameters of empirical or physical material models for metal cutting, different experiment types such as conventional tensile and compression tests, high speed Hopkinson bar tests or cutting tests can be used. The method of using high strain rate tests (split Hopkinson bar test etc.) to produce flow stress data and fitting that data to the defined material constitutive equations is widely used in impact and crash simulations. However for the machining or cutting simulation, the method of using cutting experiments to obtain material parameters is more prevalent [46]. A summary literature survey about experiment types used for obtaining material parameters is presented in Table 9 for dynamic processes.

Besides the numerical problems and many requirements to model cutting, another difficulty is the big calculation times of the cutting process (milling, sawing, etc.) encountered in parameter identification procedures. For example, A. Maurel et al (2008) [41] presents a complete method to identify the parameters of material model for for a 304L stainless steel milling. The numerical model is based on explicit arbitrary Langrangian-Eulerian(ALE) code. The material behavior is described with Johnson Cook constitutive law and the chip formation is described with a fracture model in order to consider material separation. The study finally presents an inverse identification procedure for the determination of the material parameters. However, the method is tested firstly for oblique cutting simulation and cutting force measurement of turning due to big calculation time of the milling simulation. On the other hand, the method proposed by A. Maurel et al [41] is important due to the fact that all steps of the identification procedure are defined. The procedure starts with the measurement of cutting forces and torques with experimental setup and the low pass filtering of the experimental data. Secondly the FEM simulations are performed for the same conditions as in experiments and cutting forces are obtained also from simulations. Finally, the Response Surface Method accelerated with a Moving Least Squares Method is performed to identify the parameters based on the objective function which is defined by experimental and numerical cutting forces.

As known, there is no published scientific work about the material modeling of wood in cutting process which is capable of predicting the physical phenomena such as cutting forces. Mishnaevsky et al [47] report that the interest of researchers to the possibilities of the prediction of strength of wooden parts caused a growing activity in the micro-mechanical analysis of wood behavior. Therefore, they classify the micro-mechanical models for deformation and strength into three groups so called: cellular models, laminate models and homogenization-based as illustrated in Figure 27. In addition to deformation and strength, the classification for failure consists of three groups also: fracture mechanics-based models, lattice models and combined continuum mechanical-lattice models. However, all of these modeling techniques have some inabilities. For example the cellular models, laminate models and lattice models are adequate only at the corresponding scale level. However, the extraordinary strength of wood depends on the interplay between the deformation and strength behavior of several scale levels. On the other hand, the homogenization-based models, multi-scale discrete continuum mechanical models and combined lattice-continuum mechanical models study at several levels but they are applicable only to either elastic or undamaged materials which actually means that they are not applicable for cutting applications.

Remark: Why are the current micro-mechanical models for wood not adequate for modeling of cutting?
→ Modeling of cutting requires material removal and plastic deformation. In literature, the models which study wood at several levels are applicable only either for elastic region or undamaged materials and the applications of these models are strongly limited [47].

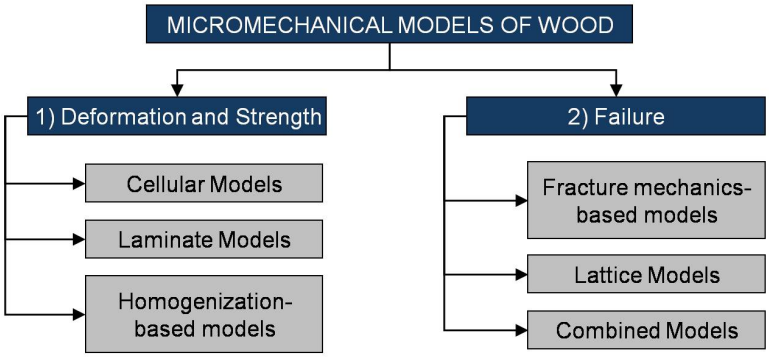

Figure 27: Classification of micro-mechanical models for deformation, strength and failure of wood (Adopted from Mishnaevsky et al [47])

One of the recent examples of the micro-mechanical modeling of wood failure is from Hofstetter et al. (2010) [48] who represent a combined random-periodic multiscale poro-micromechanics model. This study is supposed to be very the first multiscale poromechanics model related to wood strength. A summarized concept of the represented model is given in Figure 28. Due to the fact that this micromechanical model is also not applicable for cutting processes yet (like all the micro-mechanical models) the details are not given and the reference is made to Hofstetter et al [48] for further information.

Apart of recent approaches of micro-mechanical modeling, one of the examples of macro-mechanical material modeling of wood is published in Manual for Ls-Dyna [8] (Ls-Dyna is a commercial FE Code). The material model is based on number of formulations

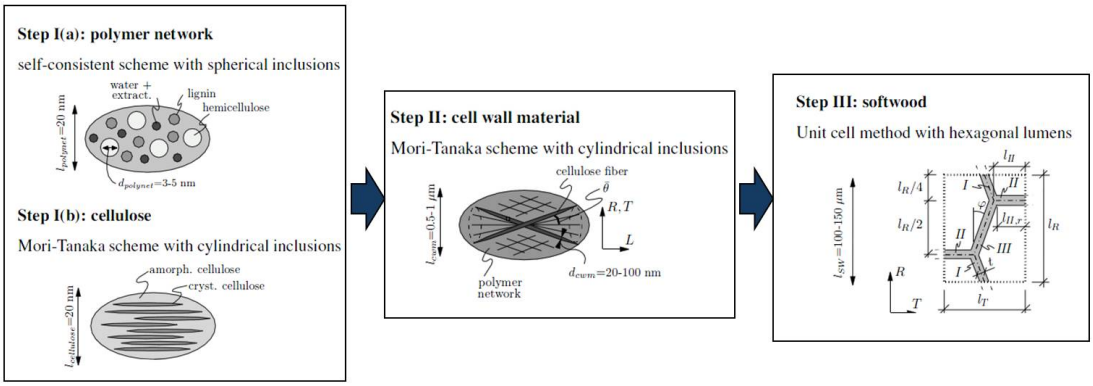

Figure 28: The micromechanical model of Hofstetter et al. [48] : Four step homogenization scheme on three hierarchical levels (from Hofstetter et al. [48])

which consists of:

a) Elastic constitutive equations,
b) Plastic flow,
c) Hardening,
d) Postpeak softening,
e) Strain-rate enhancement,
f) Failure criteria.

The elastic part for the wood model of Ls-Dyna [8] is characterized by linear elastic formulation of transversely isotropic material (see Section 2.1.2 for detailed information for elastic formulation of a transversely isotropic material). The failure criteria are the reduced form of the Modified Hashin Criteria. Plastic flow is modeled by partitioning stress and strain tensors into elastic and plastic parts with return mapping algorithms (see the Ls-Dyna Manual [8] for the information about hardening, softening, strain rate dependency and detailed information). Based on these formulations, the user can choose either to supply the material parameters or use one of the two default models of wood specimens Douglas Fir and Southern Yellow Pine. In the first option, the user has to supply 29 parameters (See Figure 10) which can be obtained by several different experiments. If one of the default models for Douglas Fir or Souther Yellow Pine is chosen, the user has to define only some properties (temperature, moisture, etc.) of the chosen specimens. The model is especially designed for impact simulations and requires a large of number of parameters for the specimens except Douglas Fir and Southern Yellow Pine. In the evaluation Manual of the Ls-Dyna model [49], conflicts on some numerical instabilities of the model are mentioned.

Table 10: Number of parameters to be supplied for wood model of Ls-Dyna [8]

	Number of parameters to be supplied
Elastic equations	5
Strength for yield criteria	6
Hardening	4
Softening	8
Strain rate	6

3.2 Material Models in Abaqus library

Abaqus consists of three main analysis products called: Abaqus Standard, Abaqus Explicit, and Abaqus CFD. Abaqus Explicit is a special-purpose analysis product that uses an explicit dynamic finite element formulation. It is suitable for modeling brief, transient dynamic events, such as impact and blast problems, and is also very efficient for highly nonlinear problems involving changing contact conditions, such as forming simulations [27]. Abaqus Explicit is chosen as analysis program in this study because of the high nonlinearity of the wood cutting and the suitability of explicit FEM formulation on dynamic problems such as cutting.

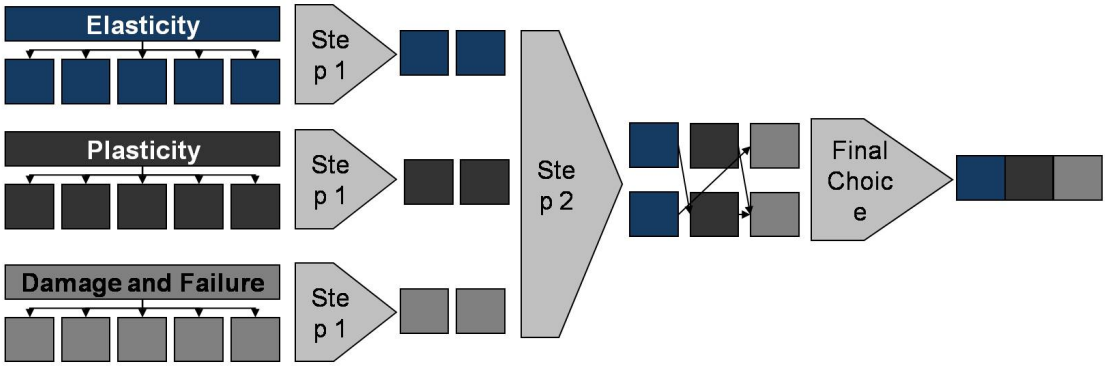

Figure 29: Analysis procedure for material models in ABAQUS

The purpose of this section is to analyze the material models available in Abaqus library and to choose the most convenient one in regard to wood cutting. In this manner, the analysis criteria are firstly determined based on the requirements for modeling of wood cutting which is previously investigated in Section 3.1. The criteria used to choose most convenient model consist of following features

1) The ability to model wood characteristics
   a) Anisotropy
   b) Hardening
   c) Strain rate dependency
   d) Temperature and moisture dependency
   e) Structural aspects (micro or ultra structure)
2) The ability to model cutting
   a) Chip formation and element removal

b) Availability in high strain rates
3) Computational costs

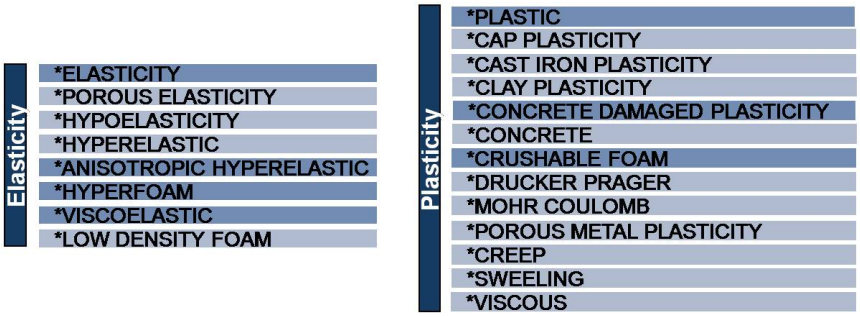

Figure 30: Material models for elasticity and plasticity available in ABAQUS

The material models in Abaqus can be classified into elasticity, plasticity and damage, in which some of them can be used in conjunction to each other. In this manner, the analysis procedure consists of two steps which are also illustrated in Figure 29. In the first step the models are evaluated in three groups so called elastic models, plastic models and the models for damage/failure. In the second step the combination possibilities of the chosen models from these three groups are evaluated in a so called flow chart and the combined models are evaluated in regard to wood cutting requirements and computational costs which leads to choose the best possible model for wood cutting. According to this procedure, the available material models in elasticity and plasticity are presented in Figure 30 while the modeling methods of damage and failure are presented Figure 31.

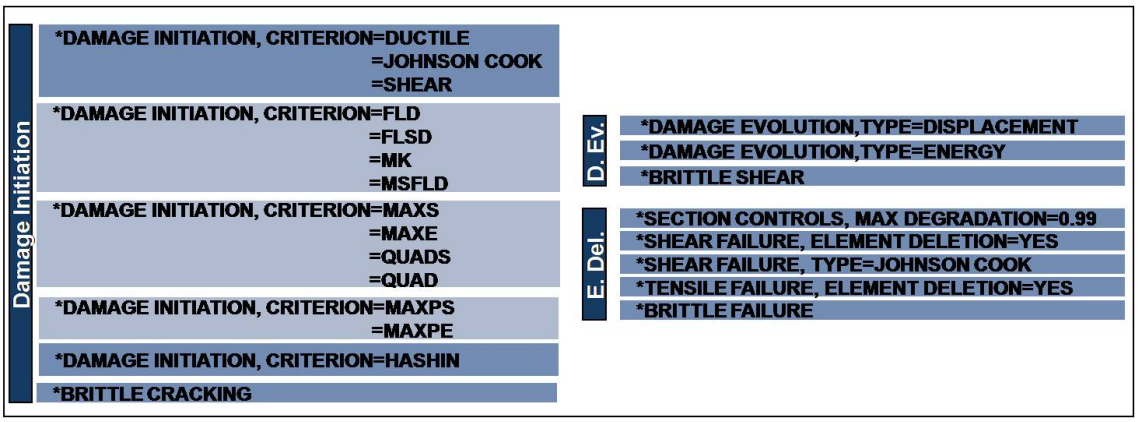

Figure 31: Material models for damage and failure available in ABAQUS

Concerning the material models presented in Figures 30 and 31, the first step and the second step of choosing procedure is performed and the results are presented in Appendix A.2. This Appendix gives a comprehensive overview to the material models in Abaqus and evaluates the models in regard to wood cutting.

In the first step, four of eight most applicable **elasticity models** are selected. These selected models are linear elasticity behavior (*ELASTICITY), anisotropic hyperelastic behavior (*ANISOTROPIC HYPERELASTIC), hyperelastic behavior in elastomeric

foams (*HYPERFOAM) and time domain viscoelasticity (*VISCOELASTIC). *ELASTICITY and *ANISOTROPIC HYPERELASTIC models enable to define anisotropy of material. However, the particular reason of selection of *ANISOTROPIC HYPERELASTIC bases on the fact that it provides a general capability for modeling materials such as biomedical soft tissues and fiber-reinforced elastomers. These materials may be assumed to be similar to wood concerning to anisotropic and fiber-reinforced structure. *HYPERFOAM model provides an isotropic and nonlinear behavior and its selection reason is the fact that it is valid for cellular solids and it enables to define compression/tension dependency. Last but not least, *VISCOELASTIC model describes isotropic rate-dependent material behavior. Thirteen most applicable **plasticity models** are also evaluated and three of them selected. The first one is the group of classical metal plasticity models (*PLASTIC) which uses Mises or Hill yield surfaces with associated plastic flow. Johnson Cook model, the most commonly used material model in metal cutting [46], belongs to *PLASTIC models also. The second and third selected models are the concrete damaged plasticity model (*CONCRETE DAMAGED PLASTICITY) and the crushable foam plasticity mode (*CRUSHABLE FOAM). It should be noted that *CRUSHABLE FOAM model is already used by Qiao et al [50] (2010) in order to model wood material for drop tests. For **Damage and Failure**, 3 sets of damage initiation and 3 damage evolution models are selected (see Figure 64 in Appendix A.2). One of them is damage and failure model for fiber-reinforced composites so called Hashin damage (*DAMAGE INITIATION, CRITERION=HASHIN). It enables to model damage for elastic-brittle materials with anisotropic behavior. Besides, two dynamic failure models (*SHEAR FAILURE and *TENSILE FAILURE) are also selected. These dynamic failure models are only available in Abaqus/Explicit and suitable only for high-strain-rate dynamic problems such as cutting.

In the second step as shown in Figure 65 in Appendix A.2, a comprehensive flow chart is designed in order to see the combination possibilities of selected models for elasticity, plasticity, damage and failure. The three elasticity models *HYPERFOAM, *ANISOTROPIC HYPERELASTIC and *VISCOELASTIC (the last 3 three rows in the flow chart in Figure 65 are have to be eliminated at the first hand due to the fact that these models are not capable to model failure. In same manner, the crushable foam plasticity model (*CRUSHABLE FOAM) and the concrete damaged plasticity model (*CONCRETE DAMAGED PLASTICITY) do not enable failure and therefore they have to be also eliminated. The two damage models, the cracking model for concrete (*BRITTLE CRACKING, *BRITTLE SHEAR and *BRITTLE FAILURE) and Hashin damage (*DAMAGE INITIATION, CRITERION=HASHIN), are not capable of modeling strain rate effects and they are eliminated too. Therefore the six combinations of models (the last 6 rows in the flow chart in Figure 65) are eliminated because of the fact that they are not able to model failure or strain rate effects. In this manner, the first four combinations of models (the first 4 rows in the flow chart in Figure 65) are the only combinations which are capable of modeling both failure and strain rate effects. Concerning these four models, the final choice is consist of Johnson Cook plasticity model (*PLASTIC HARDENING=Johnson Cook, *Rate Dependent, type=Johnson Cook) and Johnson Cook shear failure model (*SHEAR FAILURE, Type=Johnson Cook). It should be considered that the final choice is based on the following reasons:

1) Johnson Cook plasticity model comprehensively enables to model the hardening and strain-rate effects and it is capable of modeling high strain rate conditions. It should be reminded that it is the most commonly used material model in metal cutting simulation [46] and it is recently used also for cutting simulations for cortical bones (2009) [43].

2) Johnson Cook shear failure model is particularly designed for high strain rate conditions and it is compression/tension dependent.

Besides the explanations above and the explanations in the Appendix A.2, the reference is made to Abaqus Manual [27] for further investigations particularly on non-selected models.

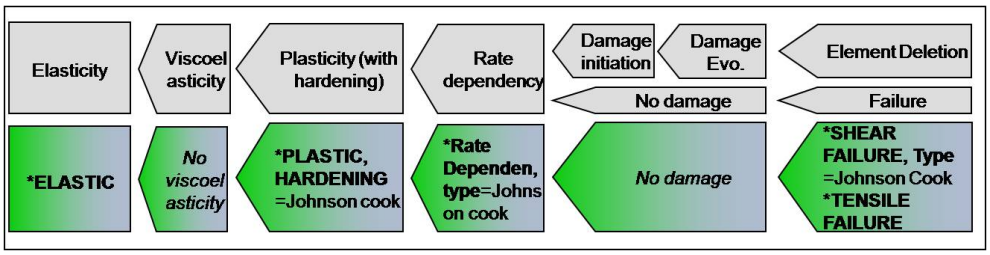

Figure 32: The representative structure of the chosen material model

Finally based on the evaluations explained above and in Appendix A.2, the material model which combines the linear elasticity, Johnson Cook plasticity and the Johnson Cook Shear Failure is chosen in order to model the behavior of wood for cutting processes as presented in Figure 32. The reason of choice for Johnson Cook Shear Failure instead of Tensile Failure is due to compression/tension dependency of Johnson Cook Shear Failure. All the specifications of the proposed model are introduced in detail in Section 3.3.

3.3 Proposed Material Model

The material model for wood cutting process consists of elastic and plastic parts and it is conjuncted with failure model in order to define material removal. The elastic part is defined with linear elasticity. Rewriting the Equation 1 from Section 2.1.2

$$\sigma = C\varepsilon \tag{48}$$

leads to the following relation between von Mises equivalent stress σ_v and von Mises equivalent strain ε_v

$$\sigma_v = E\varepsilon_v \tag{49}$$

where E is the modulus of elasticity. The plastic part is defined by the adiabatic version of Johnson Cook Flow Stress model with:

$$\sigma_v = [A + B(\varepsilon^p)^n] \left[1 + C\ln(\dot{\varepsilon^{p*}})\right] \tag{50}$$

where A, B, c and n are material parameters and ε^p refers to von Mises equivalent plastic strain. Finally, the failure is defined by adiabatic version of Johnson Cook Shear Failure Criterion:

$$\varepsilon^p_{failure} = \left[d_1 + d_2 e^{\left(d_3 \frac{p}{q}\right)}\right] \left[1 + d_4 ln\left(\frac{\dot{\varepsilon^p}}{\dot{\varepsilon_0}}\right)\right] \tag{51}$$

where d_1, d_2, d_3, and d_4 are material parameters and $\varepsilon^p_{failure}$ defines the plastic strain value at which the material fails. Disadvantageously, the proposed model is not capable to model following characteristics of wooden material

1) Anisotropy of wood
2) Temperature and moisture dependency of wood in elastic and plastic region and also at failure
3) Compression/tension dependency of wood in elastic and plastic region

However, the model is adequate for high dynamic calculations as it is explained in Section 3.2 and it is capable of defining hardening and strain rate dependency in plastic region and at failure. The failure criterion of the proposed model is also compression/tension dependent. It should be also considered that temperature dependency can be easily added to Johnson Cook Flow Stress model and Shear Failure Criterion with an additional parameter in Abaqus. The capabilities of proposed model are presented in Table 11. However in this table, the criterion "anisotrophy" is not needed for a homogeneous wooden material due to fact it is assumed as an isotropic material.

Table 11: The capabilities of proposed model

	Elastic	**Plastic**	**Fracture/Failure**
Anisotropy	-	-	-
Compression/tension dep.	-	-	√
Strain Rate dep.	-	√	√
Hardening effect	-	√	√
Temperature/moisture dep.	-	-	-

Since the proposed model defines the flow stress (von Mises stress), the effect of change of model parameters and the dependency of strain rate and compression/tension can be presented in the stress-strain curve based on the formulations of linear elasticity, Johnson Cook Plasticity Flow Stress model and Johnson Cook Shear Failure model. A possible stress-strain curve based on the parameters given in Table 12 is presented Figure 33. In Figure 33, the purple curve presents elastic region and the orange curve presents the plastic region of the material behavior. Additionally, three points represented by blue rectangular, turquoise circle and green triangular are the limits where the corresponding element fails and is excluded from the calculations for the further steps in case of uniaxial compression, uniaxial tension and pure shear respectively.

Table 12: The parameters used to define the curve in Figure 33

Lin. Elasticity		**JC Plasticity**				**JC Shear Failure**			
E (Mpa)	ν	A	B	n	C	d_1	d_2	d_3	d_4
1600	0.33	10	7	0.9	0.001	0.01	0.01	3	0.1

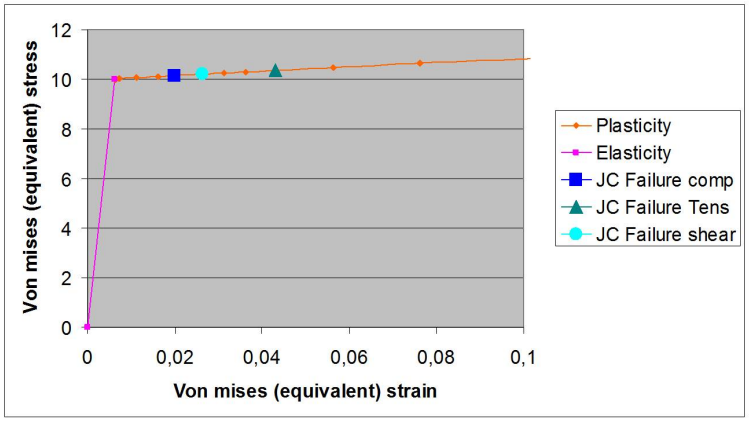

Figure 33: Stress-Strain curve for the parameters in Table 12

The detection of the failure point on the stress-strain curve is based on the stress triaxiality η

$$\eta = \frac{p}{\sigma_v} \tag{52}$$

where p and q represent hydrostatic pressure and von Mises stress respectively. The magnitude of stress triaxiality η can be used to understand whether the material is under

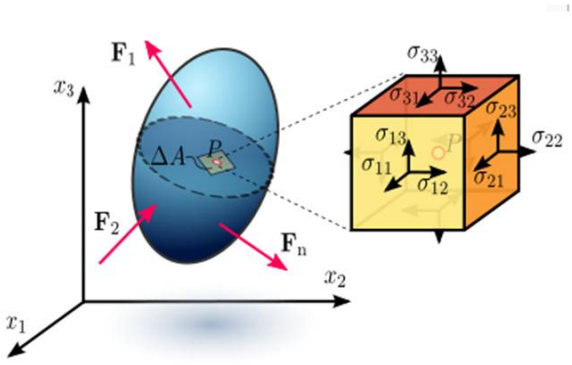

Figure 34: Components of stress tensor (from wikipedia [51])

compression, tension or shear. Regarding the definition of stress in a loaded deformable material body (see Figure 34), the stress tensor is defined as

$$\sigma = \begin{bmatrix} \sigma_{11} & \sigma_{12} & \sigma_{13} \\ \sigma_{21} & \sigma_{22} & \sigma_{23} \\ \sigma_{31} & \sigma_{32} & \sigma_{33} \end{bmatrix} \tag{53}$$

Therefore, the stress tensor for a material that is under pure tension in direction 1 can be written as:

$$\sigma = \begin{bmatrix} k & 0 & 0 \\ 0 & 0 & 0 \\ 0 & 0 & 0 \end{bmatrix}. \tag{54}$$

On the other hand, the von Mises stress σ_v and hydrostatic pressure p are defined respectively:

$$\sigma_v = \sqrt{\frac{1}{2}[(\sigma_{11} - \sigma_{22})^2 + (\sigma_{22} - \sigma_{33})^2 + (\sigma_{11} - \sigma_{33})^2 + 6(\sigma_{12}^2 + \sigma_{23}^2 + \sigma_{31}^2)]}, \tag{55}$$

$$p = -\frac{1}{2}(\sigma_{11} + \sigma_{22} + \sigma_{33}). \tag{56}$$

Therefore, based on the Equation 54, the von Mises stress σ_v and hydrostatic pressure p in case of uniaxial tension are calculated as follows:

$$\sigma_v^{uni.tension} = \sqrt{\frac{1}{2}[(k-0)^2 + (0-0)^2 + (k-0)^2 + 6(0^2 + 0^2 + 0^2)]} = k, \tag{57}$$

$$p^{uni.tension} = \frac{1}{3}(k + 0 + 0) = \frac{k}{3}. \tag{58}$$

Therefore stress triaxiality η from Equation 52 can be calculated as:

$$\eta^{uni.tension} = \frac{p^{uni.tension}}{\sigma_v^{uni.tension}} = \frac{k}{3} \cdot \frac{1}{k} = \frac{1}{3}. \tag{59}$$

In the same manner, stress triaxiality η for uniaxial compression, uniaxial compression, pures shear and biaxial tension are calculated and the results are presented in Table 13.

Table 13: Stress triaxiality magnitudes for different cases

	biaxial compression	uniaxial compression	biaxial tension	uniaxial tension	pure shear
η	$-\frac{2}{3}$	$-\frac{1}{3}$	$\frac{2}{3}$	$\frac{1}{3}$	0

Regarding the Table 13, the magnitude of stress triaxility gives the information if the material is under tension, compression or shear. This dependency makes the Johnson Cook Shear Failure Criterion also loading type dependent (tension, compression or shear) because Johnson Cook Shear Failure criterion is stress triaxiality dependent. Going back to the identification method of failure points in the stress-strain curve (see Figure 33), an example calculation is performed for uniaxial tension. Recalling the Equation 51 and using the material parameters given in Table 12, the plastic strain at which material fails is calculated:

$$\varepsilon^p_{failure-uni.tension} = \left[d_1 + d_2 e^{\left(d_3 \frac{p}{q}\right)}\right] \left[1 + d_4 ln\left(\frac{\dot{\varepsilon^p}}{,}\dot{\varepsilon_0}\right)\right] \tag{60}$$

$$\varepsilon^p_{failure-uni.tension} = \left[0.01 + 0.01 e^{\left(3\frac{1}{3}\right)}\right] \left[1 + 0.1 ln\left(\frac{1}{1}\right)\right] = 0.037 \tag{61}$$

where $\dot{\varepsilon_0}$ and $\dot{\varepsilon^p}$ are taken as 1 s^{-1}. In this manner, the corresponding plastic strain values of the whole range are presented in Figure 35.

In order to see the effect of the parameters, every parameter is variated at 3 values and the results are plotted in Figure 36. The variation of parameter A is performed at three values: 10, 18, and 26 MPa. All the other parameters are like shown in Table 12 and strain rate is taken as 1 s^{-1}. The parameter A defines the yield stress in quasi-static deformations. The larger the parameter A is, the later the plasticity starts.

In Figure 36, the variation of parameter B is done at also three values: 7, 107 and 207. All the other parameters are like shown in Table 12 and strain rate is taken as 1 s^{-1}. The

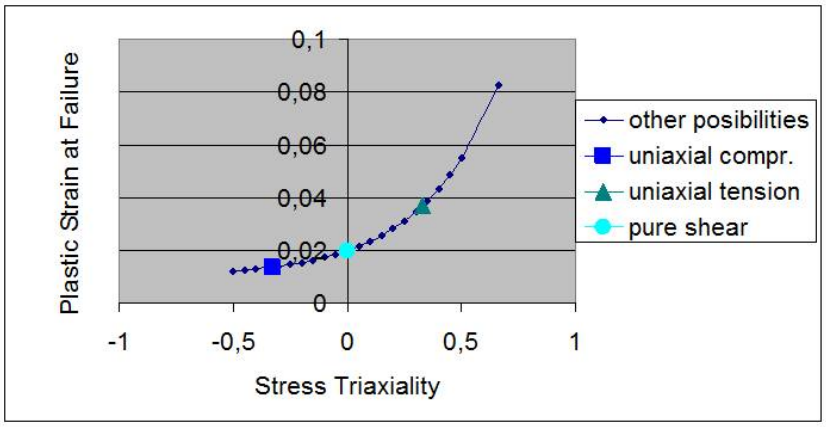

Figure 35: The relation between the stress triaxiality and the strain rate at failure

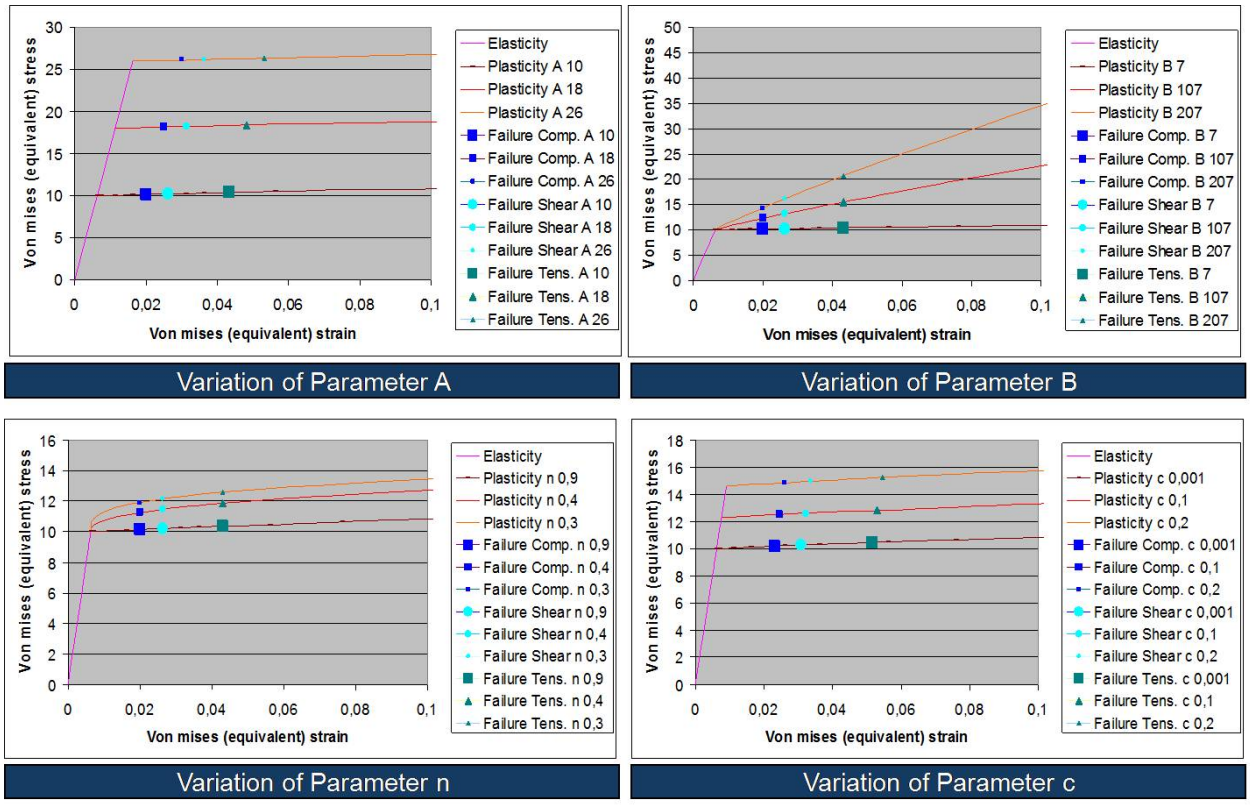

Figure 36: The variation of parameters for the proposed model

parameter B defines the hardening effect with parameter n. The larger the parameter B, the larger the slope of the curve in the plastic region. The variation of parameter n is performed at 0.3, 0.4, and 0.9 where all the other parameters are like shown in Table 12 and strain rate is taken as 1 s^{-1}. Due to the fact that plastic strain ε^p stays between 0 and 1, the larger the parameter n, the smaller the stress in plastic region. In order to see the effect of parameter C, the strain rate is taken as 10 s^{-1} while all the other parameters are defined concerning the Table 12. The strength of the material is increased when the value of parameter C is increased.

The strain rate dependency of the proposed model can be proved with plotting stress-

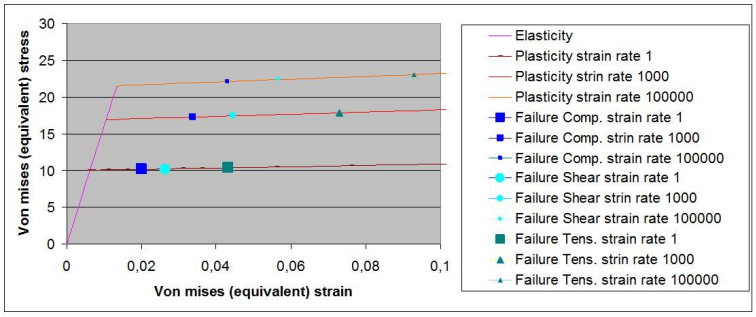

Figure 37: Stress-Strain curves at different strain rates

strain curves at different strain rates. Figure 37 presents the three curves taken at different strain rates $1s^{-1}$, $1000s^{-1}$ and $100000s^{-1}$. Figure 37 shows that the strength of the material is increased when higher value of strain rate is applied. It should be noted that the magnitudes of plastic strain at failure are also changed by the different strain rates.

It should be noted that the parameter A is taken as 10 MPa in the further sections in order to reduce the number of parameters for the optimization process.

4 Numerical Model

4.1 General Definition

Abaqus/CAE [27], an interactive environment is used to develop the Finite Element model of wood cutting, to submit the analyses of models and evaluate the results. The FE calculations are performed with Abaqus/Explicit [27], an explicit dynamics Finite Element program, and post processing of the results is done with Abaqus/Viewer [27], a subset of Abaqus/CAE.

The FEA simulation of cutting of homogeneous wooden material with router under cutting condition illustrated in Figure 38 is carried out as 2D mechanical analysis under plane strain assumption in Lagrangian approach.

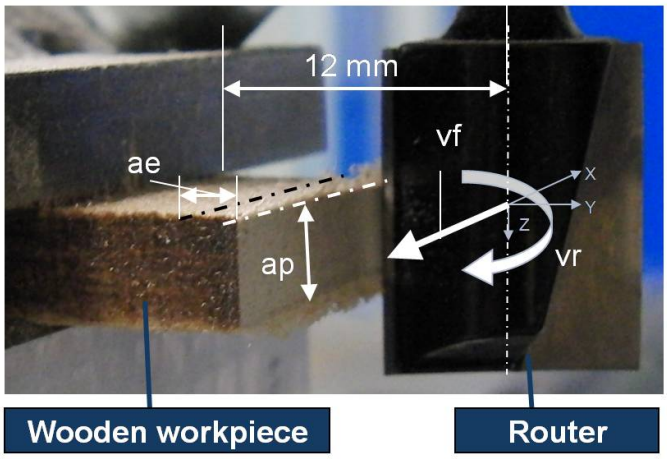

Figure 38: Cutting conditions

In cutting simulations, the wooden workpiece is stationary and the tool is moving with a constant feed velocity (vf). The model of router is discretized into 2-node 2D linear rigid elements with 1 mm global mesh size as shown in Figure 39.

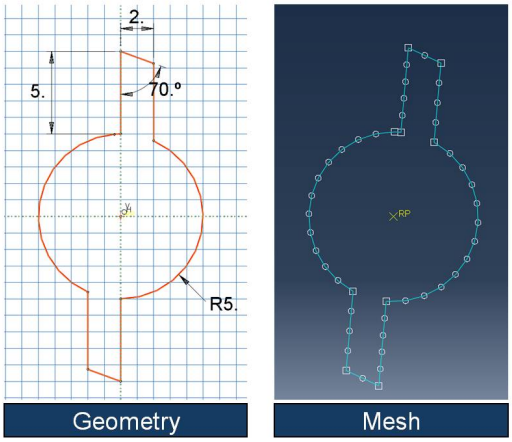

Figure 39: Geometry and meshing of model for router

One of the most critical points of the wood modeling is to determine the initial geometry of the wood. Due to the fact that only one cutting period for one blade of router is aimed to be simulated, the initial geometry of wooden workpiece is developed based on the conditions of router. In this manner, initial geometry of wood is calculated in regard to path of so called "previous cut". "Previous cut" is not simulated but illustrated in such a way that the path geometry is calculated which leads to determination of initial geometry for simulation. The illustration of "previous cut" is presented in Figure 40.

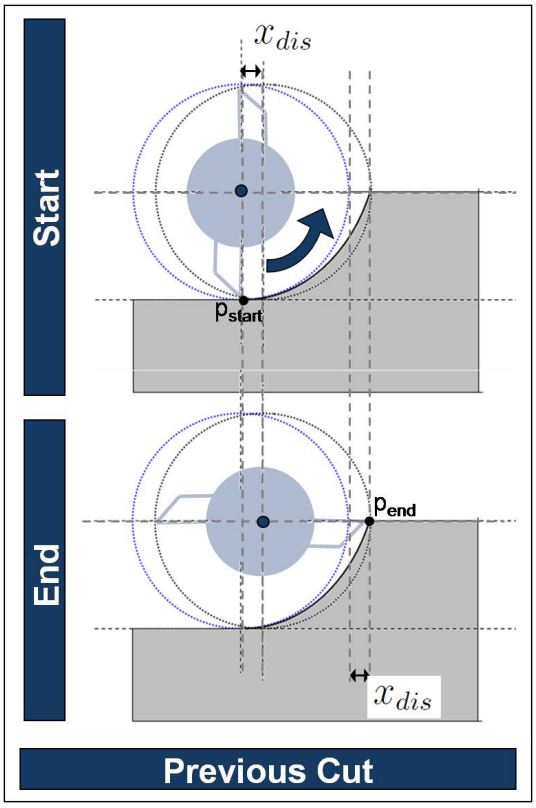

Figure 40: The start and end positions of previous cut

The dislocation of router during one period of one blade cutting is calculated concerning the cutting conditions and the angle of cutting α. The angle of cutting is defined as the angle between the points at which the interaction of the blade-workpiece starts and ends (see Figure 42). Therefore the dislocation of router is calculated with:

$$x_{dis} = \frac{1}{\frac{v_r}{60}} \cdot \frac{\alpha}{360} \cdot \frac{v_f}{60} \tag{62}$$

In order to generate the structure of path on the wood surface, an arc is constructed getting through start point p_{start}, end point p_{end} and middle point p_{middle} as shown in Figure 42. The location of p_{middle} is defined as the point which has the horizontally equidistant distances to the p_{start} and p_{end} and equidistant vertical distances to the circles on which the p_{start} and p_{end} are based (see Figure 41). With this path generated with such a method, it is aimed to apply the experimental conditions as good as possible and the cutting force curves in simulations are expected to be more qualified.

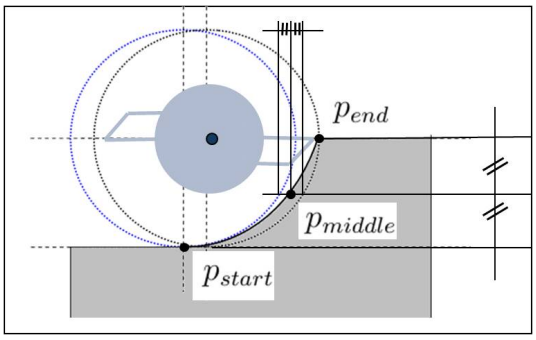

Figure 41: The location of middle point to generate arc

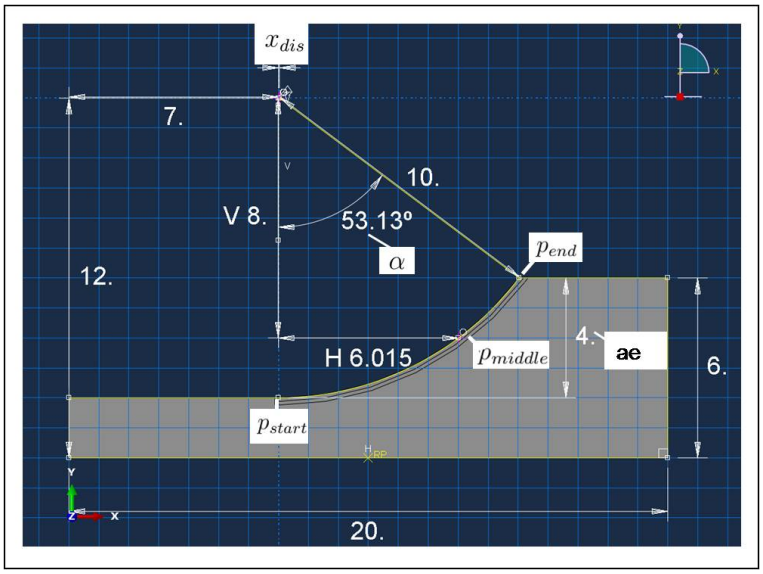

Figure 42: The Geomtry of wooden workpiece

In order to choose the element type of the model for wooden workpiece, all the available plane strain elements in Abaqus 2D solid element library are analyzed. In between 16 element types, only two of them are adequate for Abaqus/Explict: 3-node linear (CPE3) and 4-node bilinear, reduced integration with hourglass control (CPE4R). The element type is chosen as CPE3 because of the fact that CPE4SR causes very large artificial strain energy in cutting simulation. It is known that the artificial strain energy should stay negligible compared to real energies such as the strain energy and the kinetic energy [27]. A more detailed information about artificial strain energy is given Section 4.2.

The part of wooden workpiece is divided into 3 sections (See Figure 43) due to reducing the number of elements in mesh domain by the methodology of using different mesh sizes in corresponding sections. So called "cutting region" is the first section at which the wooden workpiece and router have contact and element separation appears. Because of the fact that cutting region would require the finest mesh, this section is constructed as small as possible. How much the blade get inside into the wooden material in one period of cutting is calculated as:

$$x_{mat} = \frac{1}{\frac{v_r}{60}} \cdot \frac{180}{360} \cdot \frac{v_r}{60} \tag{63}$$

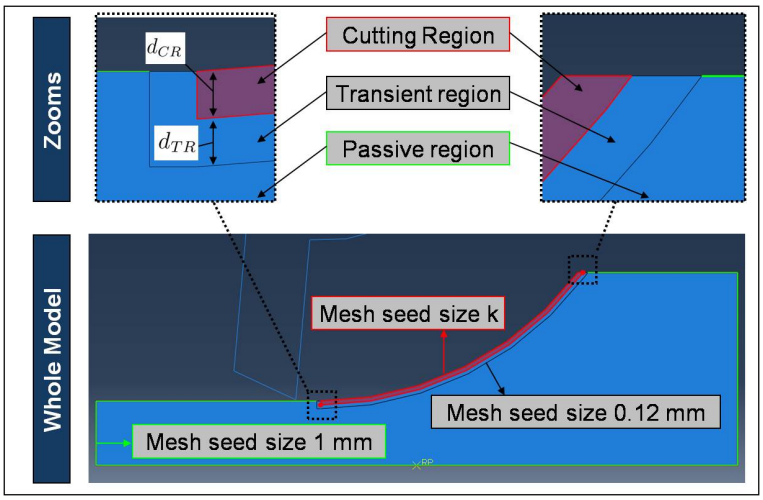

Figure 43: Sections and seeded edges

It should be considered the x_{mat} is not dependent on α but on 180^o due to the fact that router keeps dislocation also in idle state. Therefore the thickness of the cutting region d_{CR} is chosen slightly larger than x_{dis}. The purpose of using transition region is to reduce of the angle of the corner for the elements which are located on the borders of regions. In order to perform a robust mesh convergence analysis, the seed size of the all edges of cutting region "k" is chosen as objective and the other edges are seeded either 0.1 mm or 1 mm as shown in Figure 43. According to results of mesh convergence analysis, the magnitude of k is chosen as 0.04 mm. The detailed information about mesh convergence is explained in Section 4.3. It should be noted that the calculation time of the cutting is calculated based on the cutting angle α. Due to the starting angle of 5^o, the calculation time $t_{cut.all}$ is formulated as:

$$t_{cut.all} = t_{cut} + t_5 + t_{2.5} \tag{64}$$

where $t_{2.5}$ comes from the fact that it is aimed to finish calculation 2.5^o after the contact ends.

4.2 Artificial Strain Energy

In explicit dynamic analysis, energy output is an important criterion in order to check the accuracy of the solution. In general, artificial energies should stay neglible compared to real energies such as strain energy (ALLSE) and kinetic energy (ALLKE) [27] (The namings in brackets indicate the nomenclature of the Abaqus. See Table 14 for whole namings). In this manner, the artificial energies to be controlled can be artificial strain energy (ALLAE), damping dissipation (ALLVD) and the mass scaling work (ALLMW). In the finite element model described in Section 4.1, the mass scaling work stays zero because mass scaling is not used in the simulation. Therefore, the critical energies remain as artificial strain energy (ALLAE) and damping dissipation (ALLVD). The comparison of artificial energies with real energies is presented in Figure 44

Regarding to comparison in Figure 44, the analysis is based on the ratios of artificial

Table 14: Energies to be considered for the evalautuion on accuracy of the model

	Name	**Type**
ALLWK	External work	Real
ALLPD	Plastic Dissipation	Real
ALLAE	Artificial Strain Energy	Artificial
ALLKE	Kinetic Energy	Real
ALLSE	Strain Energy	Real
ALLVD	Viscous Dissipation	Artifical

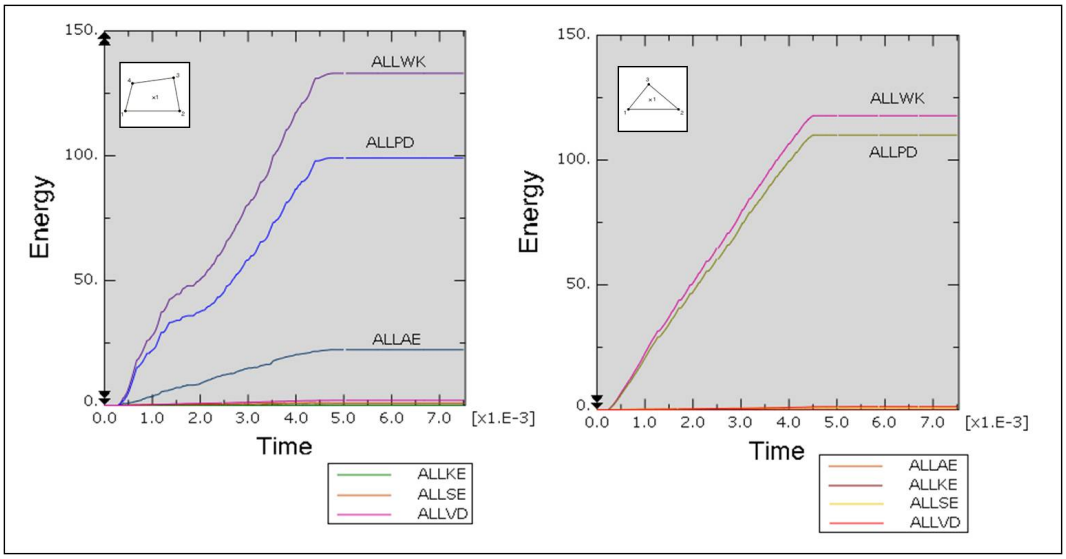

Figure 44: Energy comparison of element type CPE3 and CPE4R

energies ALLAE and ALLVD to ALLPD respectively. In this manner, the model of rectangular element (CPE4R) has relatively very high ratios which can not be neglected as presented in Table 15. However, the model of triangular element (CPE3) has very low ratios which are negligible.

Table 15: The comparison of rectangular and triangular element

Element Type	**Ratio: ALLAE to ALLPD**	**Ratio: ALLVD to ALLPD**
Rectangular CPE4R	%22	%2
Triangular CPE3	%0	%1

It should be noted that artificial strain energy includes energy stored in hourglass resistances and the reason of high artificial strain energy in CPE4R elements is due to hourglass controlling in the element formulation. Since the CPE4R element have only one integration point, it is possible to distort in such a way that the strains calculated at the integration point are all zero, which leads to uncontrolled distortion of the mesh called hourglassing [27]. Three of the possible ways of reducing artificial strain energy in the elements with hourglassing control are refining the mesh, rounding the impacting corner and reducing the stiffness of hourglassing control. However, in this problem the strategies of rounding the corner and reducing the stiffness for hourglassing control reduce the

artificial strain energy relatively little and the strategy of refining the mesh is numerically expensive. Therefore, the element type CPE3 remains as the only way to reduce artificial strain energy in cutting simulation as presented in Table 15 and 16.

Table 16: Strageties to reduce ALLAE ratio for rectangular elements

Strategy	**Ratio: ALLAE to ALLPD**	**Ratio: ALLVD to ALLPD**
-	%22	%2
Round the corner	%18	%2
Viscous Stiffness:0.1	%10	%2

4.3 Mesh Convergence Studies

The aim of mesh convergence analysis is to decide the optimum mesh size in the cutting region as previously shown in Figure 43. Due to the fact that the parameters of material model are not known yet, two different sets of material models are applied as presented in Table 17 and the analysis is based on both results.

Table 17: Two material models

	Lin. Elasticity		**JC Plasticity**				**JC Shear Failure**			
	E (Mpa)	ν	A	B	n	C	d_1	d_2	d_3	d_4
v1	1600	0.33	10	7	0.9	0.001	0.01	0.01	3	0.1
v2	1600	0.33	10	60	0.05	0.2	0.001	0.02	2	0.1

The mesh sizes and calculation times of convergence studies are presented in Table 18 for two versions of material models. The calculation times are based according to 2 processors of Intel^R Xeon^R CPU X5677 with 3.47 GHz, 1600 MHz and 48 GB Ram.

Table 18: The calculation times of different mesh sizes

	Mesh Size (mm)	**Completion**	**Calculation Time**
v1	0.06	%100	14 min 23 s
	0.04	%100	30 min 39 s
	0.03	%100	50 min 28 s
	0.02	%100	8 h 22 min 22 s
	0.01	%21.3	3 h 47 min 23 s
	0.005	%9.0	13 h 44 min 59 s
v2	0.06	%100	11 min 50 s
	0.04	%100	24 min 54 s
	0.03	%100	29 min 22 s
	0.02	%100	4 h 43 min 26 s

In order to compare the effect of different mesh sizes, the cutting force curves of every variation are plotted regarding to the process explained in Section 4.4 and results are

plotted in Figure 46 for two versions of material parameters. These two different sets of parameters represent two different material characteristics: a ductile one and a stiff one as shown in Figure 45 although the specific values of the each parameter is selected arbitrarily.

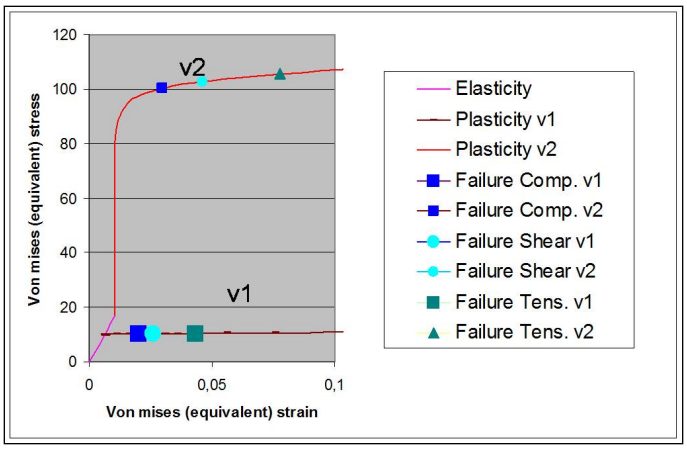

Figure 45: Stress-Strain Curves of parameters v1 and v2

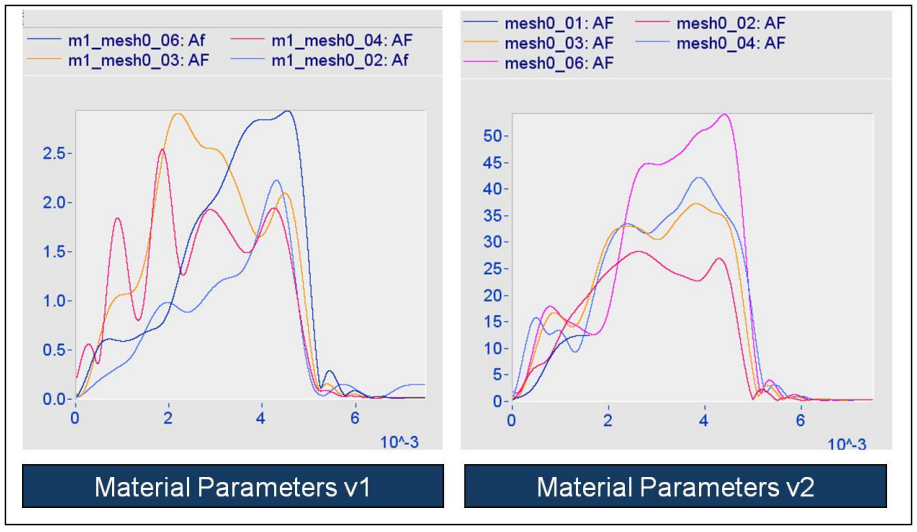

Figure 46: Compare of active forces for 0.06, 0.04, 0.03 and 0.02 mm

The oscillations are higher in v1 than in v2 because of the fact that parameters v2 represent a stiffer material behavior in comparison to parameters v1. This can be seen on the stress-strain curves of both versions as presented in Figure 45. Concerning the results presented in Figures 45 and 46, the effect of mesh dependency can be see more clearly in stiffer materials with finer mesh. The cutting forces decrease with finer mesh. It should be noted that the mesh size has not a converged value in the range 0.06 mm to 0.02 mm but the mesh size of 0.04 is chosen in regard to calculation times because of the fact that a large number of simulations is needed in the optimization process (Section 5).

4.4 Filtering of Cutting Forces

In order to calculate the cutting force occurring during wood-blade interaction, the components of the cutting force in X and Y directions should be measured both in experiments and simulations. The X and Y components of cutting force, F_X and F_Y, have larger amplitude oscillations in simulation compared to the experimental values. This difference is shown in figure 47 where the oscillations in simulation reaches both negative and positive values.

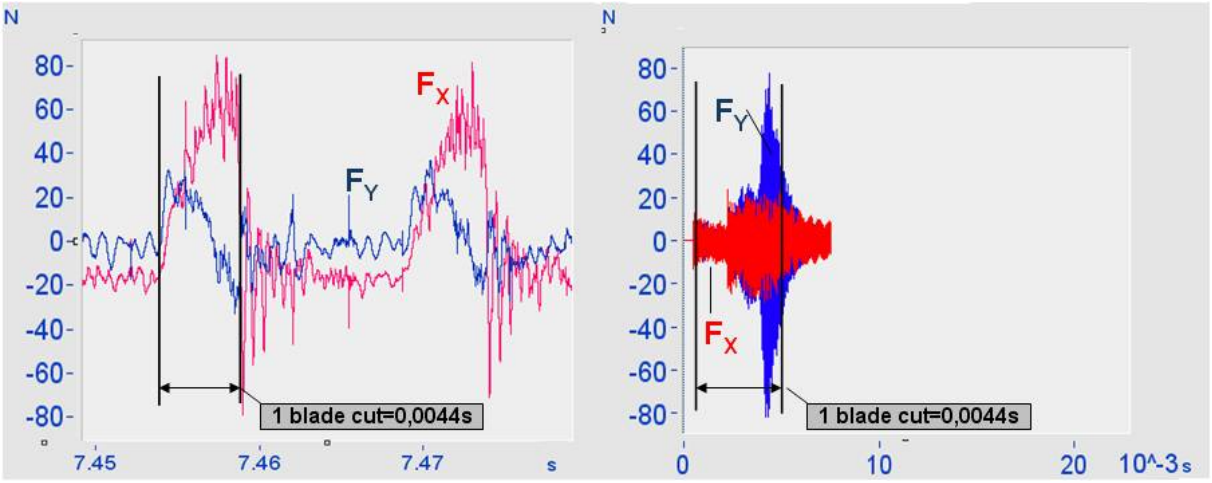

Figure 47: Overview of oscillations at F_X and F_Y in experiment (left) and simulation(right)

In order to calculate the active forces accurately, the oscillations of F_X and F_Y should be filtered. However, the cutoff frequency to perform filtering should be decided correctly. Therefore, the sources of these large oscillations of the simulation are identified firstly in order to decide the cut-off frequency of the filter. The frequencies which describe the cutting phenomenon should not be filtered. In this manner, the decision procedure is based on the method illustrated in Figure 48

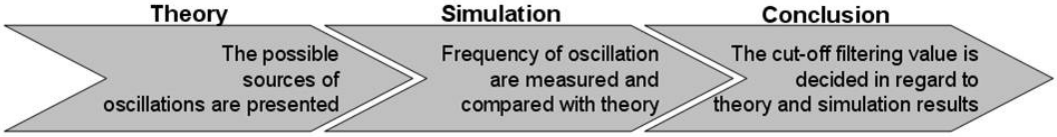

Figure 48: The decision procedure for filtering cutting forces

It is assumed that there are two types of excitations that could stimulate oscillations in the wooden material. These are

1) The excitation of the whole material which actually depends on cutting time of blade,
2) Excitation of mesh elements which are deleted during the interaction with blade.

The oscillation of first type excitation could be calculated as

$$f_{\text{materialcut}} = \frac{1}{2 \cdot \text{loading time}} = \frac{1}{2 \cdot 0,0044s} \approx 112 \text{ Hz} \tag{65}$$

where the magnitude 2 come from the fact that a system is expected to oscillate at magnitude of $\frac{1}{2 \cdot loading\ time}$ as illustrated in figure 49

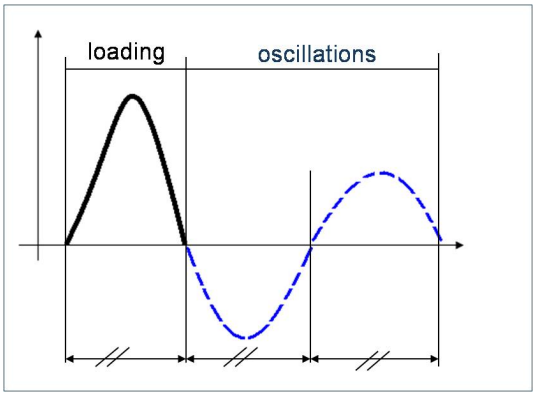

Figure 49: Oscillations

The main source of oscillations in the simulation is dependent on the deletion of each element. The frequencies of these oscillations can be estimated from the stress-time curves of the elements which are deleted in cutting process. The active loading time of every single element gives the individual frequency of the element and adds up to the oscillation frequencies of the mesh. Every element has a different active loading time and therefore the deletion of every element causes a different oscillation. Active loading times of some elements deleted in cutting processes are shown in Figure 50.

In regard to active loading times shown in figure 50 the frequency of the oscillation, $f_{elementdeletion}$, caused by element no 2167 can be calculated as following

$$f^{2167}_{\text{elementdeletion}} = \frac{1}{2 \cdot \text{loading time}} = 0.5 \frac{1}{0,0000006s} \approx 83000\text{Hz}. \tag{66}$$

In the same manner, the frequency of oscillation caused by element no 1483, $f^{1483}_{elementdeletion}$, would be 33000Hz. In order to give an idea of the range of the frequencies caused by different elements, Table 19 gives an overview about the global excitation frequency caused by one cutting period (type 1) and some of the possible numerical frequencies that could appear due to element deletions (type 2).

These examples in Table 19 show that every element has a specific element loading attitude depending on the mesh and orientation of the element. Therefore, the wood sample is stimulated by different numerous excitation frequencies depending on the specific element deletion of every element in the mesh. Considering the excitation frequencies of element deletions have a lower and upper limits, f_{lower} and f_{upper}, these limits can be constrained as

$$f_{lower} \leq f^{1483}_{elementdeletion} < f^{1741}_{elementdeletion} \leq f_{upper}, \tag{67}$$

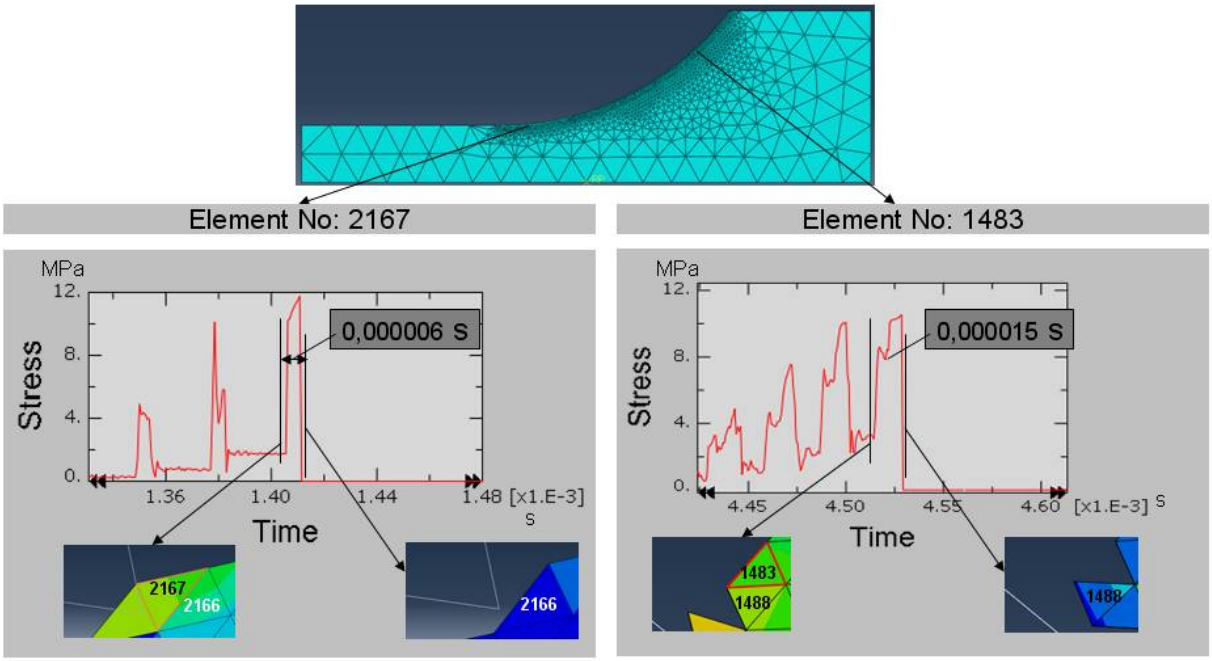

Figure 50: Loadings of elements

Table 19: Overview of Frequencies

Type	**The source of excitation**		**Frequency of oscillation**
1	Material cutting per blade		112 Hz
2	0.06 Mesh size Element deletions	element 2167	83000 Hz
		element 1483	33000 Hz
		element 1956	95000 Hz
		element 1752	83000 Hz
		element 1741	167000 Hz
		element 1969	166000 Hz

$$f_{lower} \leq 33000Hz < 167000Hz \leq f_{upper}. \tag{68}$$

It should be also considered that the possible composition of all different excitation frequencies could also create new excitation frequencies. Therefore as a hypothesis, it may be concluded that wood material is stimulated with numerous different excitations (at least at number of the deleted elements) and these excitations cause the oscillations in the cutting forces, F_X and F_Y. Moreover, the reason of large amplitude of these oscillations may be because of the fact that the material is in resonance due to the excitations of element deletions.

Next, eigenvalue extraction procedure with Abaqus/Standard for the models with 0.02 and 0.06 mm is performed respectively in order to calculate natural frequencies and the corresponding mode shapes of the wooden part. Both analyses give the same result (with a difference less than %0,1) which indicates the natural frequencies (calculated up to 200000 Hz) of the wooden model are 46851 Hz, 84954 Hz, 95441 Hz, 128638 Hz , 139195 Hz, 144163 Hz, 156934 Hz, 169435 Hz, 183709 Hz and 197941 Hz. These magnitudes of frequencies are expected to appear in F_X and F_Y with a large amplitude in case of

resonance.

The theory (or hypothesis) explained so far are subjected to explain the sources and magnitudes of "expected" oscillations in the cutting forces curves. Therefore the next step is Fast Fourier Analysis in order to calculate the frequencies of "real" oscillations appearing in the cutting forces curves. Figure 51 shows the frequencies of oscillations appearing in F_X of 0.002 mm mesh and 0.006 mm mesh respectively.

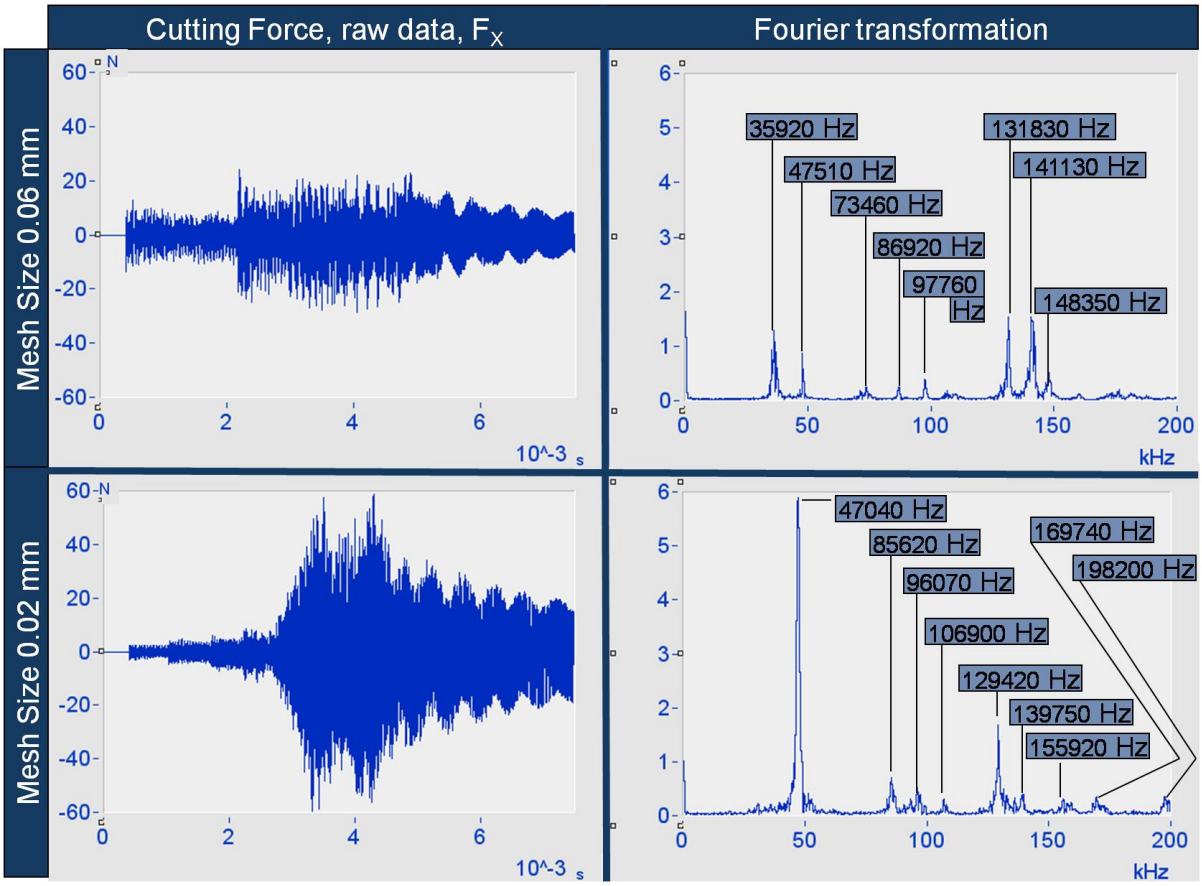

Figure 51: FFT

Comparing the magnitudes of oscillation frequencies occurring in F_X (see figure 51) with expected magnitudes (explained above), it can be concluded that the material gets into resonance due to excitation of element deletions. Considering this hypothesis and simulation results explained so far, the conclusion is made in the following box:

Summary: The oscillations on cutting forces
1) The frequency of oscillations based on cutting formation is 112 Hz and it gives the characteristic of the cutting
2) The frequencies of oscillations with large amplitudes based on element deletions are in a wide range at least from 30000 Hz to 200000 Hz and the amplitude of these oscillations may be even larger due to resonance of the material

Therefore, the frequency of 112 Hz is not wanted to be filtered. In this manner, Butterworth Lowpass with a magnitude of 1000 Hz and order of 2 is used in order to filter the numerically based oscillations generated by element deletion but not the system frequency of 112 Hz. For the future studies, it should be noted that the ways of reducing oscilla-

tions could be investigated instead of filtering them. The possible ways of this reduction could be either changing the material damping coefficient or using extended boundary conditions.

5 Parameter Identification Process

5.1 Experimental Results

The experimental results are taken via the experimental setup explained in Appendix A.3. The scheme of experimental parameters could be seen in figure 52, In this manner, Table 20 gives an overview of the experimental data that is going to be used for identification, verification and validation process.

Table 20: Overview Experiments

Process	**Case**	**ap** (mm)	**ae** (mm)	**vf** (mm/min)	**vr** (rpm)
Identification and Verification	A	ap_1	ae_1	vf_1	vr_1
	B	ap_2	ae_1	vf_1	vr_2
Validation	C	ap_1	ae_2	vf_1	vr_1
	D	ap_2	ae_3	vf_1	vr_3
	E	ap_2	ae_1	vf_2	vr_3

In identification step, two sets of experimental data (Case A and B) are intentionally used in order to identify a powerful set of parameters which could be valid for different strain rates. After the identification and verification steps are completed, the validity area of the parameters is investigated via different experimental data (Case C, D and E) where the the cutting depth, wood thickness, feed velocity and rotational velocity vary.

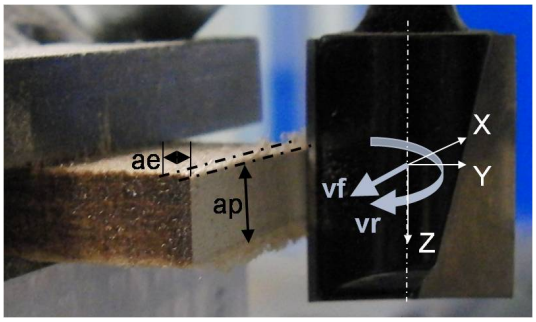

Figure 52: Experimental layout (ae: cutting depth, ap: wood thickness, vf: feed velocity, vr: rotational velocity)

The raw data of cutting forces F_X and F_Y are filtered and active force is calculated as illustrated in Figure 53. The first step is to extract one period of cutting based on one blade of router. In order to perform this extraction, one arbitrary period is chosen in every data. The decision of the starting and ending times for each case is based on the the characteristics of the curves. In order to reduce uncertainty, the starting and ending times are identified in a way that the magnitude of force is equal on these points. Next, the data of cutting forces F_X and F_Y is filtered with Low Pass of 1000 Hz and the filtered data is used in order to calculate active force. The calculation of active force is based on the equation 20. It should be considered that there is a measured force in direction of Z F_Z in experiments but it is omitted from the calculation of resultant cutting force due to the fact that it F_Z remains passive in cutting formation. In this manner, it is convenient to name the resultant force R as active force F_a (see the report of Martynenko [52] for

further details). The Famos script (Famos is a signal analysis software) of the process explained in Figures 53 and 54 are documented in Appendix A.1.

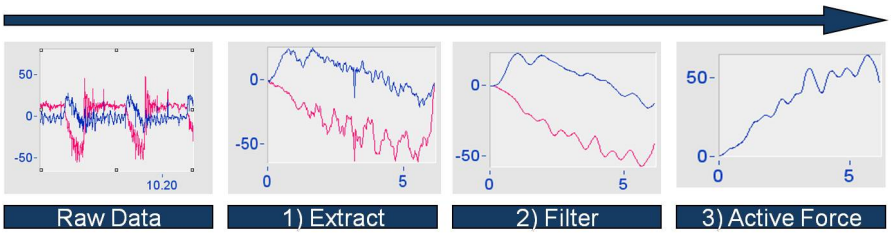

Figure 53: Experimental flow

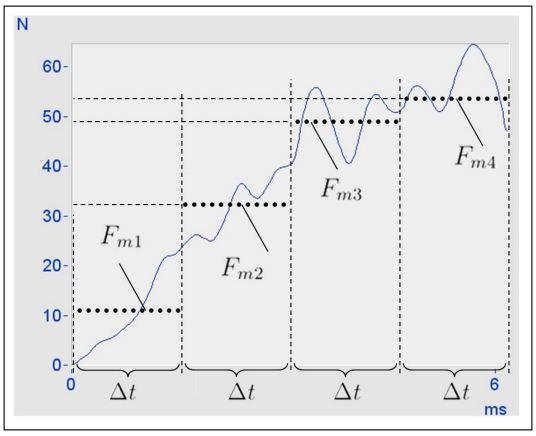

Figure 54: Calculation of mean values

After the active force is computed, the 4 mean values F_{m1}, F_{m2}, F_{m3} and F_{m4} in equidistant intervals (Δt) are calculated as illustrated in figure 54. These mean values are going to be used to build up the objective function in the identification process. Table 21 presents the mean forces of the 4 cases where the last column additionally presents the mean force magnitude of the whole cutting time F_{all} in order to give a general idea about the whole process for one cutting period (It should be noted that the case D is omitted from the calculations in this stage because an error is detected during the analysis of experimental data). Regarding to the magnitudes of F_{all} the following conclusions may be summarized as:

Remark: The effect of ap, ae, vf, vr on F_{all}
1) The larger the wood thickness (ap) is, the more the F_{all} increases
2) The larger the cutting deep (ae) is, the more the F_{all} develops
3) The greater the feed velocity (vf) is, the more the F_{all} develops
4) The greater the rotational velocity (vr) is, the less the F_{all} decreases

Table 21: Experimental Results

	ap, ae, vf, vr (mm, mm, mm/min, rpm)	$\mathbf{F}_{m1}$ (N)	$\mathbf{F}_{m2}$ (N)	$\mathbf{F}_{m3}$ (N)	$\mathbf{F}_{m4}$ (N)	$\mathbf{F}_{all}$ (N)
A	ap_1, ae_1, vf_1, vr_1	20.9	44.3	66.0	68.7	50.0
B	ap_2, ae_1, vf_1, vr_2	15.0	48.7	67.0	72.2	50.7
C	ap_1, ae_2, vf_1, vr_1	22.8	56.7	76.7	70.3	56.5
E	ap_2, ae_1, vf_2, vr_3	10.1	31.7	49.2	56.4	36.9

5.2 Finite Element Model

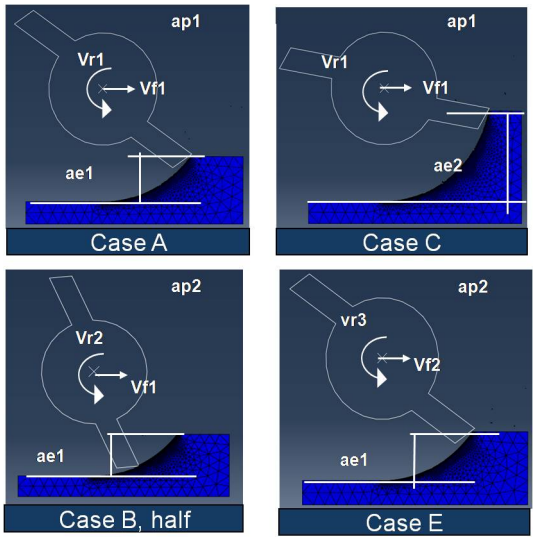

Figure 55: Initial Conditions

The finite element model is constructed based on the model explained in Section 4. Every case (previously shown in Table 20) requires its own initial geometry, initial positioning and cutting section depending on the experiment conditions. The geometries for cases A, B, C and E are presented in Figure 55. It should be noted that every case has its own x_{dis}, d_{TR} and d_{CR} as explained previously in in Section 4 (see Equations 62 - 63 and Figures 42 - 43).

5.3 Parameter Identification

In order to identify the parameters of proposed model in Section 3.3, the parameter identification procedure consisting of two steps is performed as illustrated in Figure 56. In the first step, a sampling method, in other words Design of Experiments (DOE), is applied to the design space of 7 parameters. According to the results of DOE, a new "good start" is generated for the optimization method, so called second step. A good start here means a qualified design space given by lower and upper bounds of the optimization parameters for the strategies such as response surface method or evolutionary algorithm.

Concerning the procedure explained in Figure 56, Design of Experiments is firstly performed. Design of Experiments is a sampling methodology and it can be performed with either stochastic or systematic schemes (see chapter 2.4.1 for detailed information).

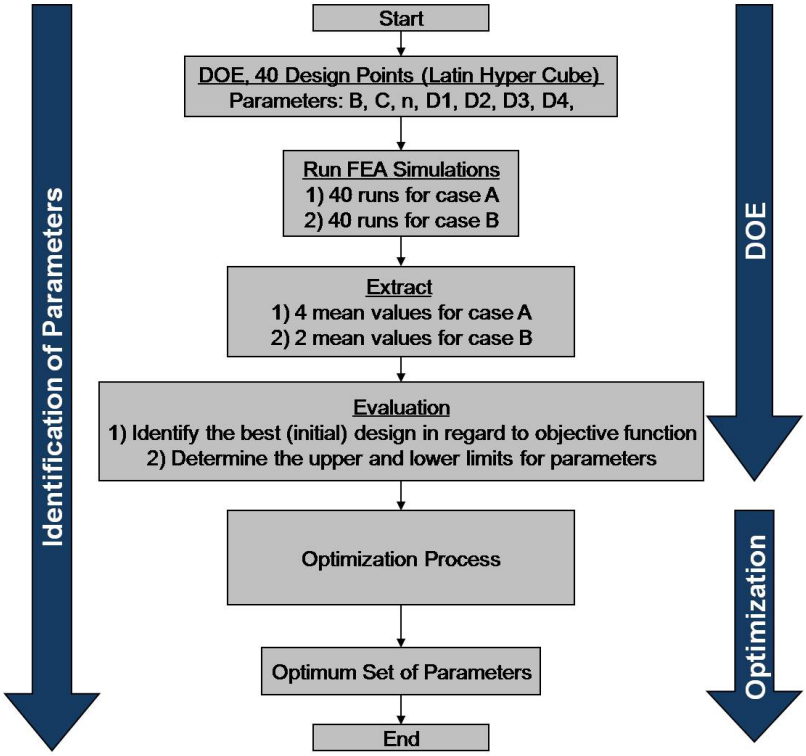

Figure 56: Parameter Identification Process

A stochastic scheme called Latin Hypercube Sampling (LHS) is chosen among the many others to perform DOE due to following reasons

Remark : The reasons of choosing LHS
A. Computational Costs in comparison to other DOE methods:
1) The most of quadratic systematic samplings methods require unacceptable number of sampling points which causes very expensive calculation time for 7 parameters (see Table 22)
2) From the 2 stochastic methods available in OptiSlang, LHS requires fewer sampling points in comparison with the other one (Monte Carlo Simulation)
B. Functionality:
1) It is the most suitable sampling method for sensitivity analysis [32]
2) It is capable to support points to create response surface

Table 22: Number of required support points for quadratic systematic sampling methodologies in case of 7 variables (adopted from [32])

Number of required support points			
Koshal	D-Optimal	Full Factorial, m=3	Central Composite
36	54	2187	143

40 support points are created by the methodology of LHS and the results are presented in Table 23 which consists of the parameters (B, n, C, d_1, d_2, d_3, d_4) and corresponding responses (F^A_{m1}, F^A_{m2}, F^A_{m3}, F^A_{m4}, F^B_{m1}, F^B_{m2}) of each design.

Table 23: LHC points

#	Design variables							Responses						Object.
	B	**n**	**C**	$\mathbf{d_1}$	$\mathbf{d_2}$	$\mathbf{d_3}$	$\mathbf{d_4}$	$\mathbf{F^A_{m1}}$	$\mathbf{F^A_{m2}}$	$\mathbf{F^A_{m3}}$	$\mathbf{F^A_{m4}}$	$\mathbf{F^B_{m1}}$	$\mathbf{F^B_{m2}}$	$\mathbf{F_{obj}}$
1	26,75	0,39	0,132	0,067	0,075	4,438	0,091	12,0	18,9	27,6	36,5	10,9	25,8	30,6
2	71,75	0,89	0,199	0,097	0,041	2,337	0,097	12,7	29,2	35,8	43,5	13,2	32,8	23,2
3	23,75	0,11	0,259	0,085	0,045	3,237	0,065	14,2	29,2	42,2	54,3	14,7	39,9	16,7
4	55,25	0,77	0,087	0,089	0,107	4,362	0,071	11,9	21,8	30,2	36,8	11,4	30,4	28,6
5	52,25	0,15	0,192	0,065	0,101	3,537	0,085	26,9	57,2	71,8	88,8	27,4	70,4	15,4
6	29,75	0,55	0,154	0,113	0,049	3,388	0,079	11,4	21,1	29,3	38,3	11,0	26,9	28,9
7	43,25	0,61	0,020	0,041	0,099	2,487	0,067	4,1	8,2	11,7	14,3	4,1	10,1	47,0
8	46,25	0,79	0,147	0,063	0,063	4,063	0,063	8,7	17,8	24,7	29,3	8,4	21,0	34,8
9	58,25	0,43	0,139	0,051	0,113	3,837	0,103	18,7	37,3	52,2	66,7	18,1	47,7	8,2
10	37,25	0,23	0,274	0,119	0,109	3,163	0,047	25,9	53,9	72,1	87,0	27,0	67,2	13,6
11	34,25	0,59	0,050	0,075	0,083	4,213	0,083	7,9	12,2	16,8	23,2	7,4	17,2	40,8
12	22,25	0,85	0,072	0,043	0,069	3,013	0,093	4,3	7,3	10,0	12,6	4,1	9,5	48,4
13	67,25	0,25	0,229	0,059	0,053	4,662	0,077	27,2	60,7	78,8	91,8	28,6	72,8	18,7
14	20,75	0,47	0,222	0,101	0,093	2,563	0,105	14,8	27,6	35,4	50,9	14,3	33,4	21,3
15	41,75	0,29	0,065	0,087	0,079	3,987	0,101	13,5	21,9	30,7	47,0	12,9	29,3	25,5
16	70,25	0,41	0,005	0,079	0,117	4,813	0,061	10,9	17,2	25,4	35,2	10,5	24,0	32,3
17	56,75	0,27	0,251	0,083	0,089	2,862	0,109	32,3	75,4	97,9	104,1	34,4	88,4	33,0
18	31,25	0,69	0,214	0,105	0,073	3,612	0,041	12,0	22,9	30,3	38,4	11,4	27,3	28,3
19	64,25	0,83	0,289	0,049	0,077	4,737	0,057	15,5	28,5	39,8	51,9	14,6	37,0	18,7
20	65,75	0,37	0,184	0,053	0,103	2,788	0,111	24,2	54,0	69,7	82,4	25,0	63,9	10,7
21	74,75	0,17	0,109	0,091	0,067	2,112	0,075	19,3	44,6	61,1	79,3	20,9	62,1	8,4
22	44,75	0,57	0,162	0,057	0,051	3,462	0,081	10,1	20,4	29,4	34,8	9,7	24,9	30,4
23	77,75	0,19	0,117	0,069	0,047	4,512	0,055	20,9	41,7	62,0	76,6	21,3	57,6	6,2
24	49,25	0,81	0,244	0,071	0,115	4,887	0,087	19,6	34,7	48,0	68,3	18,0	45,0	10,6
25	28,25	0,71	0,012	0,107	0,061	3,912	0,073	5,9	8,7	11,0	14,0	5,5	11,5	47,1
26	73,25	0,31	0,057	0,073	0,059	2,263	0,059	9,1	20,6	30,2	38,3	10,0	30,2	28,4
27	53,75	0,13	0,094	0,061	0,081	4,588	0,051	18,0	30,3	43,2	58,8	17,3	42,6	14,8
28	61,25	0,51	0,281	0,103	0,085	4,137	0,099	34,4	73,4	97,6	115,7	34,2	94,4	37,8
29	47,75	0,21	0,027	0,095	0,087	2,938	0,107	12,7	21,3	28,4	48,8	12,3	29,8	26,1
30	40,25	0,49	0,296	0,081	0,119	3,688	0,115	28,7	58,3	83,9	93,8	27,0	70,7	19,9
31	35,75	0,63	0,124	0,047	0,091	2,038	0,113	8,1	16,1	22,0	28,3	7,8	19,6	36,4
32	62,75	0,73	0,266	0,077	0,095	2,413	0,053	15,6	34,5	50,9	59,2	15,9	42,7	10,8
33	68,75	0,87	0,177	0,115	0,097	3,313	0,049	17,4	31,7	46,4	57,8	16,5	42,5	13,5
34	59,75	0,33	0,207	0,111	0,057	4,287	0,095	30,5	68,8	89,8	99,9	32,2	81,2	27,0
35	76,25	0,67	0,042	0,109	0,105	2,638	0,069	11,8	22,8	32,1	40,0	11,7	29,4	26,9
36	25,25	0,45	0,035	0,093	0,111	3,087	0,045	6,5	10,1	13,7	17,3	6,1	14,2	44,5
37	38,75	0,53	0,102	0,117	0,055	4,963	0,119	16,6	27,4	38,9	48,2	15,6	33,6	20,6
38	50,75	0,75	0,169	0,045	0,043	3,762	0,089	8,1	16,1	24,3	26,8	8,1	19,8	36,1
39	32,75	0,35	0,236	0,055	0,065	2,188	0,043	8,3	19,8	28,5	34,8	9,0	26,6	30,7
40	79,25	0,65	0,079	0,099	0,071	2,712	0,117	16,4	33,5	44,0	56,4	16,3	40,0	14,8

In order to evaluate the quality of the parameters in regard to cutting forces and to choose the best design, the objective function is designed concerning the experimental and simulation results:

$$F_{obj} = \sqrt{0.05(F_{m1}^{A,sim} - F_{m1}^{A,exp})^2 + 0.15(F_{m2}^{A,sim} - F_{m2}^{A,exp})^2 + 0.30(F_{m3}^{A,sim} - F_{m3}^{A,exp})^2 ... \\ ... + 0.30(F_{m4}^{A,sim} - F_{m4}^{A,exp})^2 + 0.05(F_{m1}^{B,sim} - F_{m1}^{b,exp})^2 + 0.15(F_{m2}^{B,sim} - F_{m2}^{B,exp})^2} \tag{69}$$

where subscripts *sim* and *exp* refer to simulation and experiments. The objective function is based on the difference of the mean values from experiments ($F_{m1}^{A,exp}$, $F_{m2}^{A,exp}$, $F_{m3}^{A,exp}$, $F_{m4}^{A,exp}$, $F_{m1}^{b,exp}$, $F_{m2}^{B,exp}$) and the mean values from the results of simulations ($F_{m1}^{A,sim}$, $F_{m2}^{A,sim}$, $F_{m3}^{A,sim}$, $F_{m4}^{A,sim}$, $F_{m1}^{b,sim}$, $F_{m2}^{B,sim}$). The coefficients (0.05, 0.15, 0.30) are used to increase the weight of some terms on objective function and the sum of all coefficients equals to 1.0. The largest coefficient (0.30) is used for the mean values at the second half of the cutting due to the fact that the maximum cutting force appears in the second half of cutting and it is more important to characterize the highest cutting load rather than the attitude in the first half. In this manner, Equation 69 can be rewritten according to experimental data in Table 21 as:

$$F_{obj} = \sqrt{0.05(F_{m1}^{A,sim} - 20.9)^2 + 0.15(F_{m2}^{A,sim} - 44.3)^2 + 0.30(F_{m3}^{A,sim} - 66.0)^2 ... \\ ... + 0.30(F_{m4}^{A,sim} - 68.7)^2 + 0.05(F_{m1}^{B,sim} - 15.0)^2 + 0.15(F_{m2}^{B,sim} - 48.7)^2.} \quad (70)$$

Therefore the objective function is calculated for all the design variables introduced in Table 23 in order to choose the best designs according to Equation 70. Regarding to this calculation, the best design is identified as design #23 . The second best and third best designs are #9and #21 respectively while the worst design is #12 as represented in Table 24.

Table 24: The objective function for corresponding parameters for best and worst designs

	#	B	n	C	d_1	d_2	d_3	d_4	$F_{obj}(N)$
The Best Design	**23**	77.75	0.19	0.117	0.069	0.047	4.512	0.055	**6.20**
2nd Best Design	**9**	58.25	0.43	0.139	0.051	0.113	3.837	0.103	**8.15**
3rd Best Design	**21**	74.25	0.17	0.109	0.091	0.067	2.112	0.075	**8.37**
The Worst Design	**12**	22.25	0.85	0.072	0.043	0.069	3.013	0.093	**48.36**

The initial value for the optimization process is chosen as second best design (Note that the second best is accidentally chosen instead of first best). The responses of chosen design (the 2nd best) is presented in comparison to experiments in Table 25 in order to see the quality of the parameters.

Table 25: Compare of chosen design of LHC and experiment

	F_{m1}^{A}	F_{m2}^{A}	F_{m3}^{A}	F_{m4}^{A}	F_{m1}^{B}	F_{m2}^{B}
2nd Best Design (Simulation)	18.7	37.3	52.2	66.7	18.1	47.7
Experiment	20.9	44.3	66.0	68.7	15.0	48.7

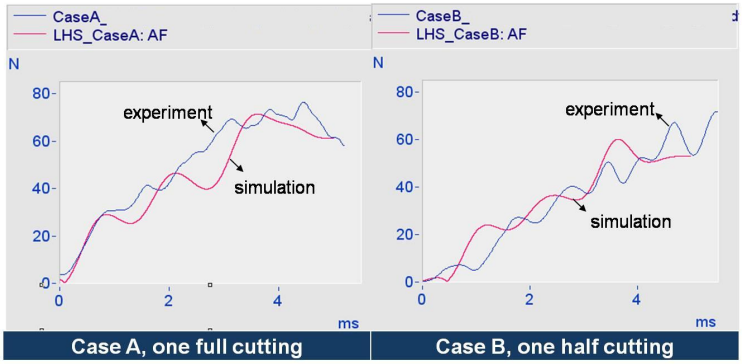

Figure 57: Compare of chosen design with experimental result for cases A and B

Besides the mean values compared in Table 25, the cutting force curves of both experiments and simulation (chosen design) are plotted in Figure 57.

Identification of the parameters for the material model are performed via 4 different methods:

Method A) Gradient based algorithm (NLQLP)
Method B) Adaptive Response Surface Method with polynomial approximation
Method C) Nature Inspired Strategy with Evolutionary Algorithm
Method D) Adaptive Response Surface Method with moving least squares approximation

Table 26: Initial parameters and lower-upper bounds for optimization methods

		B	**n**	**C**	$\mathbf{d}_1$	$\mathbf{d}_2$	$\mathbf{d}_3$	$\mathbf{d}_4$
Method A	**initial**	58.25	0.43	0.139	0.051	0.113	3.837	0.103
	lower	18.25	0.001	0.001	0.001	0.001	1.837	0.001
	upper	82.25	0.93	0.439	0.101	0.133	5.837	0.133
Method B	**initial**	58.25	0.43	0.139	0.051	0.113	3.837	0.103
	lower	18.25	0.001	0.001	0.001	0.001	1.837	0.001
	upper	82.25	0.073	0.239	0.101	0.133	4.837	0.133
Method C	**initial**	-	-	-	-	-	-	-
	lower	18.25	0.001	0.001	0.001	0.001	1.837	0.001
	upper	82.25	0.93	0.439	0.101	0.133	5.837	0.133
Method D	**initial**	58.25	0.43	0.139	0.051	0.113	3.837	0.103
	lower	18.25	0.001	0.001	0.001	0.001	1.837	0.001
	upper	82.25	0.93	0.439	0.101	0.133	5.837	0.133

The initial parameters and lower-upper bounds of these 4 methods are presented in Table 26. Since the Nature Inspired Strategy does not require any initial conditions, only upper and lower limits are introduced for this strategy.

The computational times of all these four methods are presented in Table 27. The computational time one run depends of the material parameters and it is usually between 10 minutes and 40 minutes. For example, the best design of method B lasts 15 minutes. The method B, C and D are stopped manually while the gradient based algorithm has been stopped automatically after reaching the allowed maximum number of objective function calls due to huge number of repeated designs. Method D is additionally designed as an alternative to Method B with greater upper limits. However, one of the parameters (parameter d_4) of the best design from Method D stays at the given upper limit.

Table 27: Compare of opt Methods

Method	Number of designs computed	Computational time (h)	F_{obj} (N)
A	56	18	8.15
B	63	42	3.59
C	46	42	4.16
D	29	24	4.83

The convergence behavior of the models are presented in Figure 58. It should be noted that the calculation times are limited due to the lack of time.

Although the the methods A, B, C and D are not fully completed, it is remarkable to conclude that there are many optimum sets of parameters in the design space and

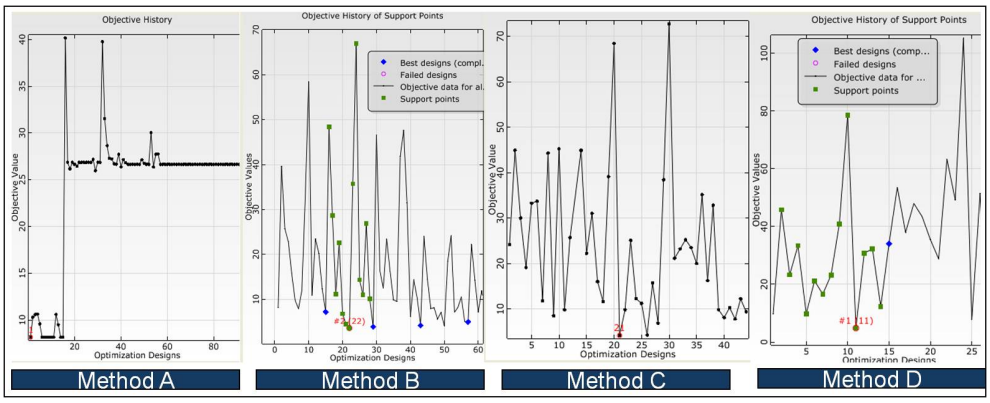

Figure 58: Convergence behaviour of the 4 methods for optimization

methods B, C and D seem to converge to different points depending on the methodology, initial values and upper-lower boundaries for parameters. In this manner, the ratios of parameters of best design to the upper and lower limits are presented in Figure 59.

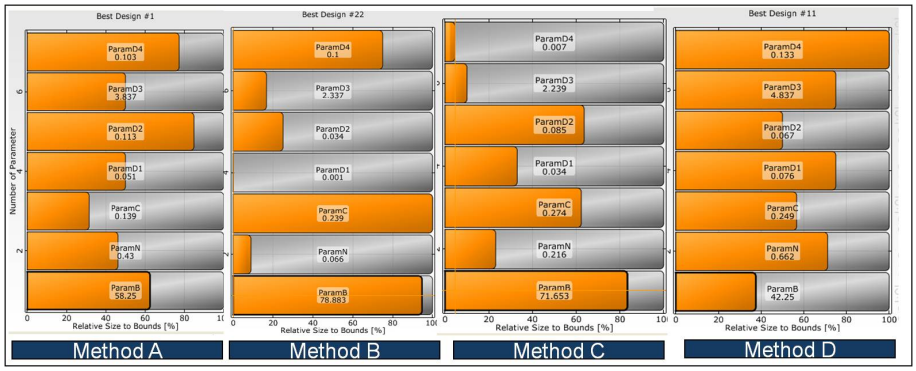

Figure 59: The ratios of parameters of best design to the upper and lower limits

Due to the fact that Adaptive Response Surface Method (Method B) has reached the minimum objective function value, the results of Method B are chosen to be evaluated and to be used for validation step (It should be noted that two parameters of best design are located on the given upper-lower limits which indicates the need of improvement for the upper-lower limits for the future work). Besides the best design of Adaptive Response Surface Method with polynomial approximation, the second best and the worst design are presented in Table 28 (see Table 30 for the complete design space of ARSM).

Table 28: The objective function for best and worst designs

	#	B	n	C	$\mathbf{d}_1$	$\mathbf{d}_2$	$\mathbf{d}_3$	$\mathbf{d}_4$	$\mathbf{F}_{obj}$
The Best Design	**22**	78,883	0.066	0.239	0.001	0.034	2.337	0.1	**3,59**
The 2nd Worst Design	**10**	74,25	0.248	0.199	0.076	0.133	3.087	0.133	**58,44**
The Worst Design	**24**	78,883	0.066	0.239	0.051	0.1	2.337	0.1	**66,94**

The difference of experimental and simulation results for F^A_{m1}, F^A_{m2}, F^A_{m3}, F^A_{m4}, F^B_{m1} and F^B_{m2} which particularly builds the objective function are presented in Table 29.

In order to verify the quality of the results, the experimental curve is compared with

Table 29: Comparison of Optimized Design of ARSM (Method B) and Experiment

	F^{A}_{m1}	F^{A}_{m2}	F^{A}_{m3}	F^{A}_{m4}	F^{B}_{m1}	F^{B}_{m2}
Optimized Simulation	18.3	45.5	63.7	66.7	19.6	56.3
Experiment	20.9	44.3	66.0	68.7	15.0	48.7

the result of optimized parameters in Figure 60. It can be seen that the model is relatively good to characterize the manner of cutting force curve.

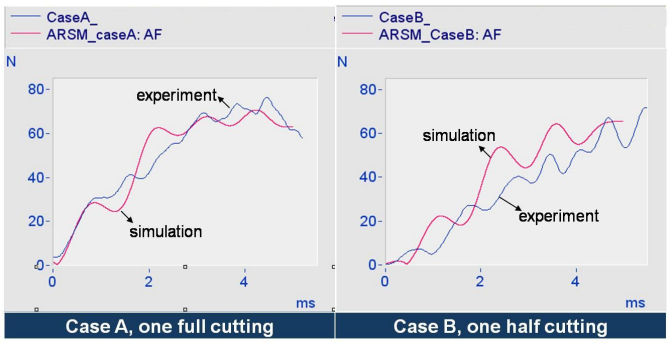

Figure 60: Comparison of optimized parameters (from Adaptive Response Surface Method with polynomial approximation) with experimental results for cases A and B

After verifying the curves as shown in Figure 60, the validation of optimized parameters is explained in Section 5.4 as next step. Additionally, the stress-strain curves of chosen model from DOE and the best design of the optimization process are presented in Figure 61. It should be noted the pre-definition of A as 10 MPa gave a realistic curve for the chosen design of DOE but not for the best design of optimization. This unrealistic curve of the best design for optimization method indicates the fact that parameter A should not be pre-defined (it should be also identified like the other parameters).

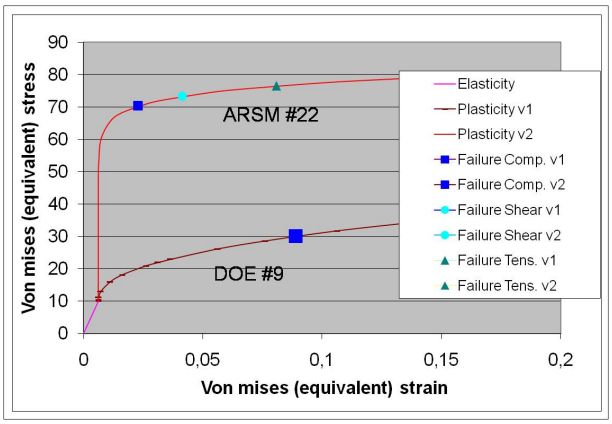

Figure 61: The stress-strain curves for the chosen model from DOE and the best design of the ARSM

Table 30: ARSM points

#	Design variables							Responses						Object.
	B	**n**	**C**	$\mathbf{d_1}$	$\mathbf{d_2}$	$\mathbf{d_3}$	$\mathbf{d_4}$	$\mathbf{F^A_{m1}}$	$\mathbf{F^A_{m2}}$	$\mathbf{F^A_{m3}}$	$\mathbf{F^A_{m4}}$	$\mathbf{F^B_{m1}}$	$\mathbf{F^B_{m2}}$	$\mathbf{F_{obj}}$
1	58,250	0,430	0,139	0,051	0,113	3,837	0,103	18,7	37,3	52,2	66,7	18,1	47,7	8,2
2	74,250	0,612	0,080	0,026	0,067	3,087	0,067	6,0	13,7	19,9	22,5	6,1	18,2	39,7
3	42,250	0,612	0,199	0,026	0,133	3,087	0,067	10,8	23,0	34,9	40,5	10,8	29,3	25,7
4	42,250	0,248	0,080	0,076	0,133	3,087	0,067	13,9	24,7	33,2	50,9	13,7	31,7	22,8
5	42,250	0,248	0,199	0,026	0,067	4,587	0,067	15,1	32,0	44,7	52,8	15,1	39,5	15,8
6	74,250	0,248	0,080	0,076	0,067	4,587	0,067	20,2	35,1	49,7	65,9	20,3	49,5	9,8
7	74,250	0,612	0,199	0,076	0,133	4,587	0,067	26,4	53,2	65,2	76,3	26,1	61,6	7,9
8	74,250	0,248	0,199	0,026	0,067	3,087	0,133	24,1	55,5	74,3	81,3	26,6	66,9	12,0
9	42,250	0,612	0,080	0,076	0,067	3,087	0,133	10,7	18,3	25,2	33,4	10,2	23,7	32,8
10	74,250	0,248	0,199	0,076	0,133	3,087	0,133	41,1	85,3	119,5	140,0	42,7	118,0	58,4
11	42,250	0,612	0,199	0,076	0,067	4,587	0,133	19,0	35,3	48,4	62,4	18,6	48,5	10,9
12	42,250	0,248	0,080	0,026	0,133	4,587	0,133	12,3	26,3	34,0	46,1	12,4	32,6	23,5
13	74,250	0,612	0,080	0,026	0,133	4,587	0,133	13,2	27,4	39,9	46,4	13,6	40,7	20,2
14	58,250	0,430	0,139	0,051	0,100	3,837	0,100	18,0	36,2	46,9	58,4	17,5	47,3	12,3
15	66,463	0,248	0,199	0,026	0,067	3,087	0,067	16,0	39,6	56,3	60,9	17,4	47,4	7,2
16	78,883	0,430	0,120	0,001	0,034	2,337	0,034	2,2	6,2	10,1	13,1	2,9	9,4	48,4
17	54,044	0,430	0,239	0,001	0,100	2,337	0,034	8,5	21,0	31,0	38,0	9,3	25,3	28,7
18	54,044	0,066	0,120	0,051	0,100	2,337	0,034	14,1	31,1	48,6	64,8	15,3	46,9	11,1
19	54,044	0,066	0,239	0,001	0,034	3,837	0,034	9,2	29,7	43,1	38,2	10,8	33,7	22,6
20	78,883	0,066	0,120	0,051	0,034	3,837	0,034	15,4	37,7	57,9	74,2	17,7	56,5	6,8
21	78,883	0,430	0,239	0,051	0,100	3,837	0,034	22,7	48,7	67,3	69,9	23,2	57,8	4,5
22	78,883	0,066	0,239	0,001	0,034	2,337	0,100	18,3	45,4	63,7	66,8	19,6	56,3	3,6
23	54,044	0,430	0,120	0,051	0,034	2,337	0,100	7,0	16,9	23,5	27,7	7,6	22,5	35,7
24	78,883	0,066	0,239	0,051	0,100	2,337	0,100	41,8	100,5	131,3	146,4	46,4	123,8	66,9
25	54,044	0,430	0,239	0,051	0,034	3,837	0,100	14,9	33,7	50,0	50,7	15,5	39,7	14,3
26	54,044	0,066	0,120	0,001	0,100	3,837	0,100	18,2	36,0	51,0	57,1	18,8	46,5	11,0
27	78,883	0,430	0,120	0,001	0,100	3,837	0,100	12,0	27,2	37,5	31,4	14,0	38,7	26,9
28	66,463	0,248	0,179	0,026	0,067	3,087	0,067	15,1	36,5	52,6	57,8	16,2	44,6	10,1
29	54,044	0,152	0,239	0,051	0,034	3,837	0,066	17,5	41,7	61,8	70,6	19,3	55,0	3,9
30	62,200	0,294	0,120	0,036	0,001	3,387	0,046	3,4	7,3	11,5	15,9	3,5	10,3	46,6
31	45,888	0,294	0,239	0,036	0,067	3,387	0,046	13,2	30,7	43,6	53,4	14,4	38,7	16,3
32	45,888	0,009	0,120	0,066	0,067	3,387	0,046	16,3	31,9	46,0	62,8	16,8	47,2	12,5
33	45,888	0,009	0,239	0,036	0,001	4,287	0,046	11,9	26,3	36,6	43,8	12,6	30,0	23,5
34	62,200	0,009	0,120	0,066	0,001	4,287	0,046	13,0	29,2	41,5	58,2	13,9	39,4	16,2
35	62,200	0,294	0,239	0,066	0,067	4,287	0,046	23,6	53,4	73,8	78,4	25,4	63,6	9,9
36	62,200	0,009	0,239	0,036	0,001	3,387	0,086	18,3	39,8	51,5	59,9	18,7	47,4	9,5
37	45,888	0,294	0,120	0,066	0,001	3,387	0,086	5,2	10,7	16,7	21,9	5,3	14,8	41,8
38	62,200	0,009	0,239	0,066	0,067	3,387	0,086	35,9	83,3	111,0	125,2	39,3	102,7	47,6
39	45,888	0,294	0,239	0,066	0,001	4,287	0,086	9,2	18,9	26,8	35,6	9,2	23,7	31,5
40	45,888	0,009	0,120	0,036	0,067	4,287	0,086	19,7	43,4	56,4	63,4	18,8	46,1	6,2
41	62,200	0,294	0,120	0,036	0,067	4,287	0,086	15,9	32,1	44,0	58,7	15,5	42,3	14,3
42	54,044	0,152	0,179	0,051	0,034	3,837	0,066	14,9	33,8	50,8	61,2	15,6	47,4	10,2
43	53,557	0,275	0,239	0,036	0,067	4,287	0,086	21,9	47,4	63,8	68,7	22,6	57,6	4,2
44	58,571	0,369	0,168	0,027	0,047	3,837	0,071	11,3	24,3	36,3	42,7	11,3	31,1	24,1
45	48,542	0,369	0,239	0,027	0,087	3,837	0,071	16,3	35,2	46,9	52,0	16,2	43,6	14,5
46	48,542	0,182	0,168	0,045	0,087	3,837	0,071	20,6	40,2	52,4	65,4	20,4	49,8	7,9
47	48,542	0,182	0,239	0,027	0,047	4,737	0,071	18,5	39,3	57,1	57,6	19,8	49,5	8,1
48	58,571	0,182	0,168	0,045	0,047	4,737	0,071	20,5	38,8	57,3	68,7	20,8	52,8	5,6
49	58,571	0,369	0,239	0,045	0,087	4,737	0,071	24,3	49,2	61,6	73,8	23,9	62,4	7,1
50	58,571	0,182	0,239	0,027	0,047	3,837	0,101	19,7	47,2	66,5	71,5	21,1	57,4	4,1
51	48,542	0,369	0,168	0,045	0,047	3,837	0,101	13,8	28,3	41,9	50,5	14,1	35,1	18,5
52	58,571	0,182	0,239	0,045	0,087	3,837	0,101	31,2	69,5	84,9	93,2	32,0	83,3	24,1
53	48,542	0,369	0,239	0,045	0,047	4,737	0,101	19,3	39,7	53,7	66,9	19,0	49,1	7,1
54	48,542	0,182	0,168	0,027	0,087	4,737	0,101	19,6	39,5	52,0	66,6	20,5	52,6	8,2
55	58,571	0,369	0,168	0,027	0,087	4,737	0,101	17,6	36,8	50,8	58,4	17,8	49,2	10,5
56	53,557	0,275	0,203	0,036	0,067	4,287	0,086	19,9	42,6	58,3	65,0	20,1	52,0	5,0
57	48,987	0,182	0,239	0,032	0,047	3,837	0,101	18,8	40,6	59,1	64,2	19,8	50,7	5,0
58	53,123	0,239	0,196	0,025	0,035	3,567	0,086	10,9	26,3	40,9	41,7	12,0	34,0	22,2
59	44,852	0,239	0,239	0,025	0,059	3,567	0,086	15,7	34,4	47,0	53,0	16,7	43,1	14,2
60	44,852	0,124	0,196	0,039	0,059	3,567	0,086	18,3	36,2	54,6	66,3	18,7	49,1	7,2
61	44,852	0,124	0,239	0,025	0,035	4,107	0,086	14,6	33,9	51,4	54,8	15,3	45,0	11,9
62	53,123	0,124	0,196	0,039	0,035	4,107	0,086	17,1	37,6	54,5	67,7	18,2	53,3	7,1

5.4 Validation

The validation of the models is based on Cases C and E as presented in Figure 55. Table 31 compares the mean cutting forces of experimental data of Case C and E with the simulation which has the optimized parameters in regard to Adaptive Response Surface Method with polynomial approximation.

Table 31: Validation for case C and E in regard to mean values of cutting forces

		$\mathbf{F_{m1}}$	$\mathbf{F_{m2}}$	$\mathbf{F_{m3}}$	$\mathbf{F_{m4}}$
C	Experiment	22.8	56.7	76.7	70.3
	Simulation	24.3	48.5	62.9	60.5
E	Experiment	10.1	31.7	49.2	56.4
	simulation	13.69	23.22	50.13	45.46

In order to have a better understanding of the comparison of experimental data and simulation, the comparison of curves for experimental data and simulation is presented in Figure 62.

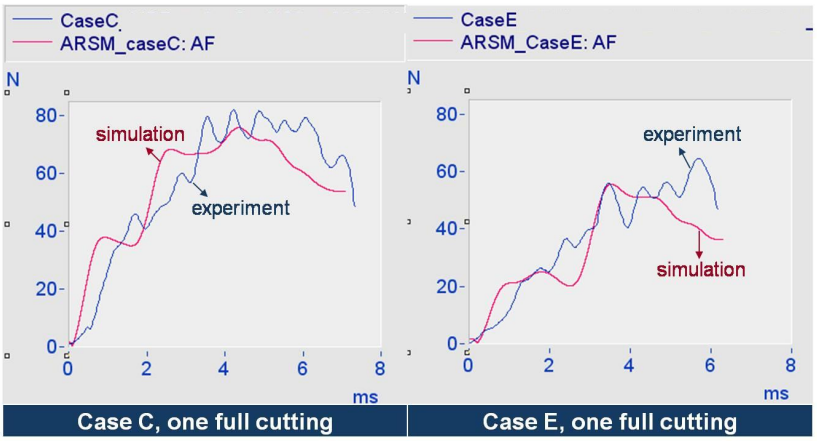

Figure 62: Validation

6 Conclusions

The master thesis presented a whole methodology which includes the material and numerical modeling, experimental analysis and parameter identification process in order to model wood cutting which is capable of predicting cutting forces. Because of the fact that good matching of experimental and simulation results (approximately 10%) (see Figure 60) would not mean that the model is accurate, the validation of the optimized parameters is investigated for different cases (see Figure 62). The matching of simulation and experimental data (approximately 20%) for different cases can mean that the model is validated in a wide range of conditions for router cutting and it indicates a potential for the other types cutting conditions. However, the following recommendations should be considered for the future work:

1) Some constraints for the parameters of proposed model should be developed regarding the estimated stress-strain curves for homogenous wooden material. This constraints on parameters
would help to get more realistic stress-strain curves from optimization process
2) The mesh convergence studies should be performed with finer meshes until the convergence is satisfied
3) High oscillations on the wooden material should be lowered with one of the methods such as using finer mesh, using material damping or extending the boundary conditions.
4) The optimization methodology should be reviewed and the design space should be identified with a new methodology including parameter sensitivity analysis.
5) The objective function should be improved including the new parameters such as chip formation.
6) The validity area of optimized parameters should be also investigated for other cutting tools.
7) The model should be transformed into thermo-mechanical one using the temperature parameters of Johnson Cook Plasticity and Shear Failure Models.
8) Parameter is not taken as 10 MPa. It should be identified with the parameter identification process as well as the other parameters.
9) 3D Finite Element modeling of cutting should be performed and the results should be compared with the 2D plane strain approximation.
10) Finally, the capability of the material model and methodology should be proved for more complex wooden materials and cutting conditions.

References

[1] Pentti O. Kettunen. *Wood, Structure and Properties.* Trans tech Publications Ltd, Switzerland, 2006.

[2] Wood Handbook. *Wood as an Engineering Material.* Forest Products Laboratory USDA Forest Service Madison, Wisconsin, 1999.

[3] Stefan Holmberg. *A Numerical and Experimental Study of Initial Defibration of Wood.* PhD thesis, Lund University, Division of Structural Mechanics, Sweeden, 1998.

[4] M. Neumann. *Investigation of the Behavior of Shock-Absorbing Structural Parts of Transport Casks Holding Radioactive Substances in Terms of Design Testing and Risk Analysis.* PhD thesis, Bergische Universitaet Wuppertal, 2009.

[5] Hans Petersson Stefan Holmberg, Kent Persson. Nonlinear mechanical behaviour and analysis of wood and fibre materials. *Computers and Structures*, 72:459–480, 1999.

[6] http://en.wikipedia.org/wiki/Wood, March 2011.

[7] Paulo Monteiro. http://www.ce.berkeley.edu/ paulmont/CE60New/wood.pdf, March 2011.

[8] Development Research and Turner-Fairbank Highway Research Center Technology. *Manual for LS-DYNA Wood Material Model 143.* U.S Department of Transportation, Publication No. FHWA-HRT-04-097,, 2007.

[9] Peter Niemz. *Holzphysik (Lecture Notes).* ETH, Institut fuer Baustoffe, Zuerich, 2006.

[10] J. Bodig and B. A. Jayne. *Mechanics of wood and wood composites.* Van Nostrand Reinhold, New York, 1982.

[11] L.J. Gibson and M. F. Ashby. *Cellular solids structure and properties.* Pergamon Press, New York, 1988.

[12] Stefanie E. Stanzl-Tschegg and Parviz Navi. Fracture behaviour of wood and its composites. a review. *Holzforschung*, 63:139–149, 2009.

[13] Winston A. Knight Geoffrey Boothroyd. *Fundamentals of Machining and Machine Tools.* Taylor and Francis Group, 2006.

[14] Eero kivimaa. *Cutting Force in wood-working.* PhD thesis, The State Institute for Technical Research, Helsinski, 1950.

[15] Norman C. Franz. *Analysis of the Wood-Cutting Proces.* University of Michigan Press, 1958.

[16] William M. McKenzie. *Fundemantel Analysis of The Wood-Cutting Process.* PhD thesis, Department of Wood Technology, University of Michigan, 1960.

[17] Louis-Erienne Denaud Bernard Thibaut Laurent Bleron Remy Marchal, Frederic Mothe. Cutting forces in wood machining - basics and applications in industrial processes. a review. *Holzforshung*, 63:157–167, 2009.

[18] http://en.wikipedia.org/wiki/Machining, 18.04.2011.

[19] http://www.bosch-pt.de, 18.04.2011.

[20] Editor Kai Cheng. *Machining Dynamics*. Springer-Verlag London Limited, 2009.

[21] George E. Woodsen and Peter Koch. *Tool forces and Chip Formation In orthogonal Cutting of Loblolly Pine*. Southern Forest Experiment Station Forest Service US . Department of Agriculture, 1970.

[22] J. Palmqvist. Parallel and normal cutting forces in peripheral milling of wood. *Holz als Roh- und Werkstoff*, 61:409–415, 2003.

[23] Peter Niemz. *Grundlagen der Holzbe- und Verarbeitung*. Lecture Notes, Swiss Federal Institute of Technology Zurich, 2007.

[24] R. Bruce Hoadley. *Understanding Wood, A CraftmanÂ ´s Guide to Wood Technology*. The Taunton press, Inc., 2000.

[25] C.Miehe. *Micromechanics of Materials and Homogenization Methods*. Lecture Notes, Univesity of Stuttgart, 2010.

[26] C.Miehe. *Theoretical and Computational Mechanics of Materials at Large Strains*. Lecture Notes, Univesity of Stuttgart, 2010.

[27] Abaqus Documentation. Abaqus 6.10 Simulia, 2011.

[28] T.J.R Hughes J.C Simo. *Computational Inelasticity*. Springer-Verlag New York, Inc, 1998.

[29] R.L Zienkiewicz, O.C. & Taylor. *Finite Element Method: Volumes 1, 2 and 3., 5th Edition*. John Wiley and Sons, 2000.

[30] Wam K. L.-Moran B. Liu W. K Belytschko, T. *Nonlinear Finite Elements for Continua and Structures*. Butterworth Heinemanns, 2000.

[31] C.Miehe. *Parameter Identification Methods and Experimental Mechanics*. Lecture Notes, Univesity of Stuttgart, 2010.

[32] Optislang Documentation. dynordo GmbH, 2011.

[33] Andreas Rieger. *Zur Parameteridentifikation komplexer Materialmodelle auf der Basis realer und virtueller Testdaten*. PhD thesis, Institut fuer Mechanik, Universitaet Stuttgart, Germany, 2005.

[34] Gerald Scheday. *Theorie und Numerik der Parameteridentifikation von Materialmodellen der finiten Elastizitaet und Inelastizitaet auf der Grundlage optischer Feldmessmethoden*. PhD thesis, Institut fuer Mechanik, Universitaet Stuttgart, Germany, 2003.

[35] H. McCallion Lan Le-Ngoc. A cellular finite element model for the cutting of softwood across the grain. *International Journal of Mechanical Sciences*, 63:157–167, 2009.

[36] M.J. King A.J. Caughley. Modelling the collapse of wood cells during the cutting process. *Holz als Roh- und Werkstoff*, 61:403–408, 2003.

[37] Lars-Erik Lindgren Ales Svoboda, Dan Wedberg. Simulation of metal cutting using a physically based plasticity model. *Modelling and Simulation in Material Science and Engineering*, 18, 2010.

[38] Lars-Erik Lindgren Vahid Kalhori, Dan Wedberg. Simulation of mechanical cutting using a physical based material model. *International Journal of Material Forming*, 3:511–514, 2010.

[39] Cook W. H Johnson G. R. A constitutive model and data for metals subjected to large strains, high strain rates and high temperatures. *7th International Symposium on Ballistics*, pages 514–546, 1983.

[40] J.C. Gelin O. Ghouati. Identification of material parameters directly from metal forming processes. *Journal of Materials Processing Technology*, 80-81:560–564, 1998.

[41] S. Thibaud1 G. Michel J.C. Gelin A. Maurel, M. Fontaine1. Experiments and fem simulations of milling performed to identify material parameters. *International Journal of Material Forming*, pages 1435–1438, 2008.

[42] L.;Micari F.;Rizzuti S.; Umbrello D. Chinesta, F.; Filice. Assesment of material models through simple machining tests. *International Jounrnal of Material Forming*, pages 507–510, 2008.

[43] A.V.;Silberschmidt V.V. Alam, K.; Mitrofanow. Finite element analysis of forces of plane cutting of cortical bone. *Computational Materials Science*, 46:738–743, 2009.

[44] Martin Baeker Aviral Shrot. Is it possible to identify johnson-cook law parameters from machining simulations? *International Journal of Material Forming*, 3:443–446, 2010.

[45] R.C. Dewesa S.L. Sooa, D.K. Aspinwall. 3d fe modelling of the cutting of inconel 718. *Journal of Materials Processing Technology*, 150:116–123, 2004.

[46] Mahmoud Al Bawaneh. *Determination of Material Constituve Models using orthogonal Machning Tests*. PhD thesis, Wichita State University, 2007.

[47] Louis-Erienne Denaud Bernard Thibaut Laurent Bleron Remy Marchal, Frederic Mothe. Micromechanical modelling of mechanical behaviour and strength of wood: State-of-the-art review. *Computational Materials Science*, 44:363–370, 2008.

[48] Christian Hellmich Thomas K. Bader, Karin Hofstetter and Josef Eberhardsteiner. Poromechanical scale transitions of failure stresses in wood: from the lignin to the spruce level. *Zeitschrift fuer Angewandte Mathematik und Mechanik*, 90:750–767, 2010.

[49] Development Research and Turner-Fairbank Highway Research Center Technology. *Evaluation of LS-DYNA Wood Material Model 143*. U.S Department of Transportation, Publication No. FHWA-HRT-04-096,, 2007.

[50] G. Wieser U. Zencker T. Quercetti L. Qiao, V. Ballheimer. Numerische simulation von fallversuchen mit behaelterstossdaempfern bei unterschiedlichen fallwinkeln mittels abaqus/explicit. *Deutsche SIMULIA-Konferenz 2010*, 20.-21. September 2010, Heidelberg, 2010.

[51] http://en.wikipedia.org/wiki/Stress_ (mechanics), 17.05.2011.

[52] Sergey Martynenko. *Beitrag zur Steigerung der Effektivitaet und Prozesssichherheit der Hoch-leisstungsbearbeitung von Holz- Holzwerkstoffen mittels Bearbeitungszentren*. Bericht, Institut fuer Werkzeugmschinen, Universitaet Stuttgart, 2007.

A Appendices

A.1 Famos Script for Experimental Data

The software Imc Famos 6.0 is used in order to analyze the signals measured from the experiments. The script written in Famos syntax is presented in Figure 63. (Please note that the second filtering value should be also 1000 Hz not 10000 Hz. This changes the results of mean values approximately %5)

Page 1

```
;; Experimental Data Analysis
;; NOTE: the sequence of data in Excel should be same with the sequence of imported raw data

Anzahl=VarGetInit(1)
;; Loading the lower and upper time limits of the signal from a given excek sheet
fh = FileOpenXLS( "C:\DATA.xls", 0)
x = FileXLSColumnRead( fh, 1, 1, Anzahl, 0)
y = FileXLSColumnRead( fh, 2, 1, Anzahl, 0)
Daten = XYvon(x,y)
index=1
solange index <= Anzahl
   TxName = VarGetName?(index)
   ;;Reading the lower and upper time limits
   start = Daten[index].x
   end = Daten[index].y
   dt=(end-start)/4
   ;;Calculation of offset value
   TxNameMean=mitte(Gren(<TxName>,(start-0.000001),start))
   ;;Cutting Out
   TxNameAS= TAdd( TxName,"AS")
   <TxNameAS>=Gren(<TxName>,start,end)
   ;;Offset
   TxNameA0= TAdd( TxName,"_A0")
   <TxNameA0>=(<TxNameAS> -TxNameMean)
   ;;Initializing the starting time
   TxNameReady= TAdd( TxName,"_Ready")
   <TxNameReady> = xOff(<TxNameAo>, 0)
   ;;Filtering with 1000Hz
   TxNameFilt= TAdd( TxNameReady,"_Filt")
   <TxNameFilt>=spieg(FiltTP(spieg(FiltTP(<TxNameReady>,0,0,2,1000)),0,0,2,10000))
   ;;Calculation of Cutting Force
   TxNameFiltAktiv= TAdd( TxNameFilt,"_Aktiv")
   <TxNameFiltAktiv>=WURZ((<TxNameFilt>:Fxp1^2)+(<TxNameFilt>:Fzp1^2))
   ;;Mean Values at Intervals
    TxNameMittel1= TAdd( TxNameFiltAktiv,"Mittel1")
   <TxNameMittel1>=Mitte(Gren(<TxNameFiltAktiv>,0,dt))
   TxNameMittel2= TAdd( TxNameFiltAktiv,"Mittel2")
   <TxNameMittel2>=Mitte(Gren(<TxNameFiltAktiv>,dt,(2*dt)))
   TxNameMittel3= TAdd( TxNameFiltAktiv,"Mittel3")
   <TxNameMittel3>=Mitte(Gren(<TxNameFiltAktiv>,(2*dt),(3*dt)))
    TxNameMittel4= TAdd( TxNameFiltAktiv,"Mittel4")
   <TxNameMittel4>=Mitte(Gren(<TxNameFiltAktiv>,(3*dt),(4*dt)))
   TxNameMittelGanz= TAdd( TxNameFiltAktiv,"MittelGanz")
   <TxNameMittelGanz>=Mitte(Gren(<TxNameFiltAktiv>,(0),(4*dt)))
   ;;Update of Index
   Tindex=("ok")
   Index = index+1
   ENTFERNEN <TxNameAS>
   ENTFERNEN <TxNameA0>
ende
```

Page 2

```
ENTFERNEN TxNameReady
ENTFERNEN Anzahl
ENTFERNEN index
ENTFERNEN Tindex
ENTFERNEN TxName
ENTFERNEN TxNameFilt
ENTFERNEN TxNameFiltAktiv
ENTFERNEN TxNameAS
ENTFERNEN TxNameA0
ENTFERNEN TxNameMean
ENTFERNEN start
ENTFERNEN end
ENTFERNEN fh
ENTFERNEN x
ENTFERNEN y
ENTFERNEN Daten
ENTFERNEN TxNameMittel1
ENTFERNEN TxNameMittel2
ENTFERNEN TxNameMittel3
ENTFERNEN TxNameMittel4
ENTFERNEN TxNameMittelGanz
ENTFERNEN dt
```

Figure 63: The script for signal analysis in Famos syntax

A.2 Methodology to choose a material model (Step 1 and 2)

The methodology to choose a material model for wood cutting from Abaqus material libraries consists of two steps which are represented in Figures 64 and 65 respectively. Figure 64 presents firstly properties of wood on the left side of the chart and then gives an overview of the material models in Abaqus on the right side in five parts: Elasticity, Plasticity, Damage Initiation, Damage Evolution and Element Deletion. The blue highlighted material cards are the chosen models of the first evaluation. In the second step, chosen models from first step are reevaluated concerning the combination possibilities with each other and the ability to model wood cutting.

Figure 64: Overview of Properties of Wood and Mechanical Material Models in Abaqus (step 1)

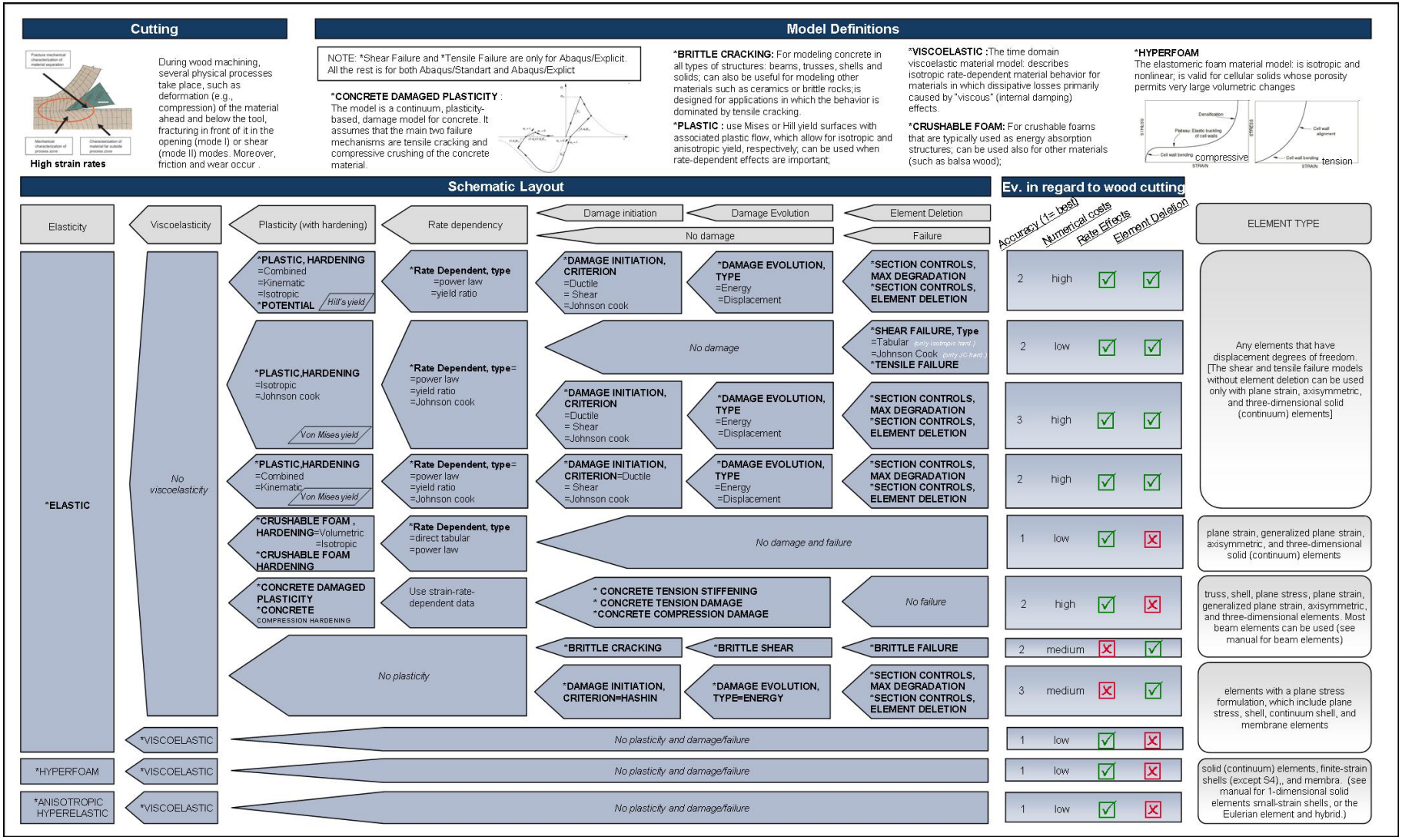

Figure 65: Evaluation of Material Models in Abaqus (Step 2)

A.3 Experimental Setup

The experimental setup consists of an ICP Chronos measurement tool, PCB Sensor and Milling Machine as illustrated in Figure 66. The raw data is converted into resultant cutting force after extracting one cutting period and filtering.

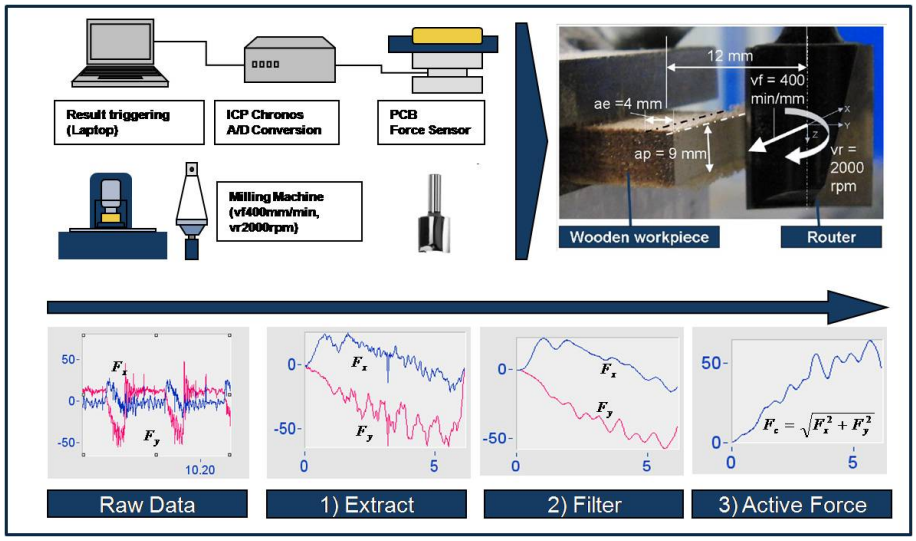

Figure 66: Experimental Setup and Signal Analysis

A.4 Excel Sheet to Produce Stress-Strain Curves for the Proposed Material Model

In order to visualize the stress-strain curves for a set of parameters of the proposed model, the calculations are performed with an excel sheet concerning the equations explained in Section 3.3. This excel sheet consists of 4 parts: Formulation, Input, Calculations and Graphics. The parts of Input and Graphics of the excel sheet are presented in Figure 67. This excel sheet is designed in order to be able to compare different set of parameters and to distinguish the effect of each parameter in a practical way.

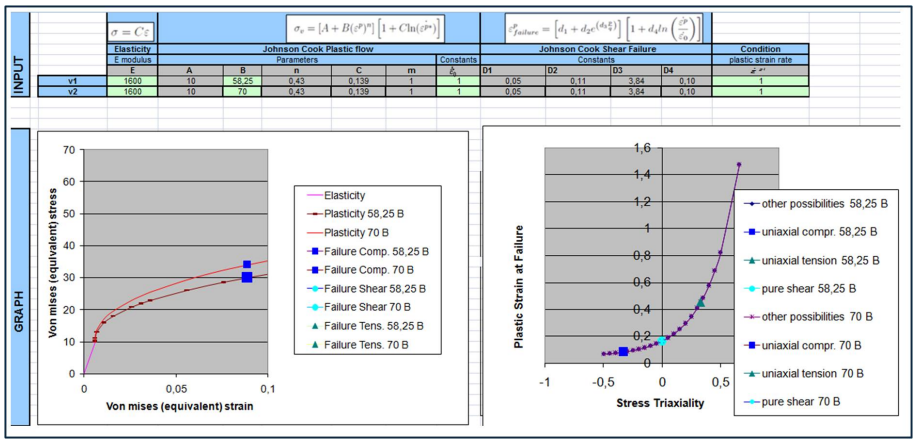

Figure 67: Excel Sheet for producing stress-strain curves for the proposed material model